

Computational Exploration of Non-Valence Anions from Biological Quinones

Mauro GASCÓN

Supervisor: Prof. T. C. Jagau
KU Leuven

Mentor: Robin Moorby
KU Leuven

Thesis presented in
fulfillment of the requirements
for the degree of Master of Science
in Theoretical Chemistry and Computational Modelling

Academic year 2024-2025

© Copyright by KU Leuven

Without written permission of the promotor and the authors it is forbidden to reproduce or adapt in any form or by any means any part of this publication. Requests for obtaining the right to reproduce or utilize parts of this publication should be addressed to KU Leuven, Faculteit Wetenschappen, Celestijnenlaan 200H bus 2100, 3001 Leuven (Heverlee), telephone +32 16 32 14 01.

A written permission of the promotor is also required to use the methods, products, schematics and programs described in this work for industrial or commercial use, and for submitting this publication in scientific contests.

This thesis is an exam document that obtained no further correction of possible errors after the defense. Referring to this thesis in papers and analogous documents is only allowed after written consent of the supervisor(s), mentioned on the title page.

Acknowledgements

Thank you thank you.

Abstract

This thesis investigates the two anionic states of ubiquinone (CoQ), a valence-bound (VBS) and non-valence dipole-bound states (DBSs). DBSs, where an excess electron is weakly bound by the molecular dipole, have sparked interest as potential ‘doorway’ states in electron transfer processes, yet their study is challenging due to their diffuse nature and sensitivity to electron correlation.

The primary theoretical framework employed is the equation-of-motion coupled-cluster (EOM-CC) theory, using the cost-effective second-order approximation, CC2. First, the EA-EOM-CC2 method for calculating electron affinities of both VBSs and DBSs anions is benchmarked and validated. Dyson orbitals for EOM-CC2 are implemented, providing a robust tool for characterizing electron attachment/detachment processes and calculating properties like photodetachment cross-sections.

Investigations on CoQ analogues, Q0 (2,3-dimethoxy-5-methyl-1,4-benzoquinone) and Q1 (CoQ with one isoprene unit), reveal a strong interplay between molecular conformation and the stability of DBSs, mediated by changes in the molecular dipole moment. The study also explored the influence of the local molecular environment on these anionic states using small cluster models.

Results demonstrate that EA-EOM-CC2, with appropriate basis sets, effectively describes both VBSs and DBSs. The newly implemented EOM-CC2 Dyson orbitals offer a reliable and computationally efficient alternative to higher-order methods. This research enhances the understanding of how structural and environmental factors govern the properties of anionic states in biologically relevant quinones, providing insights and tools for future studies in more complex systems.

Beknopte samenvatting

GET AN INDIGENOUS SPECIMEN TO CHECK THIS TRANSLATION

Deze thesis onderzoekt de twee anionische toestanden van ubiquinon (CoQ): een valentiegebonden toestand (VBS) en een niet-valentie dipoolgebonden toestand (DBS). DBS'en, waarbij een extra elektron zwak gebonden wordt door het moleculaire dipoolmoment, hebben veel interesse opgewekt als mogelijke 'doorgangstoestanden' in elektronentransferprocessen. Het bestuderen van deze toestanden is echter uitdagend door hun diffuse aard en gevoeligheid voor elektronencorrelatie.

Het theoretisch kader dat hiervoor gebruikt wordt, is de 'equation-of-motion coupled-cluster' (EOM-CC) theorie, toegepast in de kostenefficiënte tweede-orde benadering, CC2. Eerst wordt de EA-EOM-CC2 methode om elektronenaffiniteiten van zowel VBS- als DBS-anionen te berekenen, gevalideerd en gebenchmarkt. Dyson-orbitalen voor EOM-CC2 zijn geïmplementeerd, wat een krachtig hulpmiddel biedt om elektronenaanhechtings- en losmaakprocessen te karakteriseren en eigenschappen zoals fotodetacheringsdoorsneden te berekenen.

Onderzoek naar CoQ-analogen, Q0 (2,3-dimethoxy-5-methyl-1,4-benzoquinon) en Q1 (CoQ met één isopreneenheid), toont een sterk samenspel tussen de moleculaire conformatie en de stabiliteit van DBS'en, gestuurd door veranderingen in het moleculaire dipoolmoment. Ook werd de invloed van de lokale moleculaire omgeving op deze anionische toestanden onderzocht met behulp van kleine clustermodellen.

De resultaten tonen aan dat EA-EOM-CC2, met geschikte basissets, zowel VBS- als DBS-toestanden accuraat beschrijft. De nieuw geïmplementeerde EOM-CC2 Dyson-orbitalen bieden een betrouwbaar en reken efficiënt alternatief voor duurdere methodes. Dit onderzoek levert nieuwe inzichten op in hoe structurele en omgevingsfactoren de eigenschappen van anionische toestanden in biologisch relevante chinonen beïnvloeden, en biedt hulpmiddelen voor toekomstige studies in complexere systemen.

List of abbreviations

NVS Non-Valence State

DBS Dipole-Bound State

VBS Valence-Bound State

QBS Quadrupole-Bound State

CBS Correlation-Bound State

EOM Equation-of-Motion

CC Coupled Cluster

CCSD Coupled Cluster with Single and Double excitations

CC2 Second-order approximate Coupled Cluster

HF Hartree-Fock

DFT Density Functional Theory

MP2 Møller–Plesset perturbation theory of second order

CoQ Coenzyme Q

uQ Ubiquinone

Q_n Ubiquinone with n isoprene units

ETC Electron Transport Chain

MO Molecular Orbital

EA Electron Affinity

QM Quantum Mechanics

Contents

Abstract	iv
Beknopte samenvatting	v
List of abbreviations	vi
1 Introduction	1
1.1 Non-Valence Anions	1
1.1.1 Dipole-Bound Anions	2
1.1.2 Approaches to Study Non-Valence Anions	3
1.1.3 Non-Valence Anions in Condensed Matter	4
1.1.4 Non-Valence Anions in Biological Systems	4
1.2 Ubiquinone	5
1.3 Research Goals	7
2 Theoretical Background	9
2.1 Self-Consistent Field Methods	9
2.1.1 Electron Correlation	10
2.1.2 Møller-Plesset Perturbation Theory	10
2.1.3 Density Functional Theory	11
2.1.4 Configuration Interaction	11
2.1.5 Coupled Cluster Theory	12
2.1.6 Second Approximate Coupled Cluster	13
2.2 Equation-of-Motion Methods	14
2.3 Dyson Orbitals	16
2.3.1 EOM-CC2 Dyson Orbital Equations	17
3 Computational Details	19
4 Results and Discussion	21
4.1 Performance of EOM-CC2 Related Methods	21

4.1.1	Basis Set Dependence of EA-EOM-CC2 in Dipole Bound Anions	21
4.1.2	Performance of EA-EOM-CC2 on Valence Bound Radical Anion States of Quinones	24
4.1.3	Photoelectron Cross-section from EOM-CC2/CCSD	25
4.2	Study on the Anion States of Ubiquinone	26
4.2.1	Energy and Dipole Surfaces of CoQ	26
4.2.2	Interaction with small molecules	33
5	Conclusion and Outlook	36
A	Algebraic expressions for the Dyson orbitals	45
B	Photoelectron Cross-sections	48

Chapter 1

Introduction

1.1 Non-Valence Anions

An anion is an atom or molecule possessing a negative charge¹⁻⁴. The binding of electrons to a molecule is a balance between the attractive potential between the electron and the nuclei, and the repulsive forces between the electrons. Because the equilibrium of charge is broken towards the negative side, the binding energy of the excess electron is typically significantly smaller in magnitude than the ionisation energy of the neutral molecule. Moreover, the properties of the anion can be very different from those of the neutral species, with differences ranging from the structure to the chemical reactivity. In discussions of molecular anions, the concept of electron affinity (EA) is key. The adiabatic electron affinity (AEA) quantifies the energy difference between a molecule and its corresponding anion, both in their structural ground state and lowest rovibrational levels. The vertical electron affinity (VEA), defined at the neutral equilibrium geometry, is particularly relevant for electron capture dynamics. A molecule with a positive EA is considered electronically stable, requiring energy input to remove an electron from the anionic state¹.

Molecular anions are classified into valence bound states (VBS), where the excess electron occupies a compact orbital similar to valence molecular orbitals, and non-valence states (NVS), where the excess electron occupies a diffuse orbital spatially separated from the molecule. Unlike valence electrons, these “extra” electrons do not experience a $-1/r$ Coulombic attraction at long distances. Instead, they interact through charge-multipole potentials, which are weaker than the covalent bonds holding the molecule together^{1,4}.

Non-valence anions can be categorised into dipole-bound states (DBS)⁵⁻⁹, quadrupole-bound states (QBS)¹⁰⁻¹², and correlation-bound states (CBS)¹³⁻¹⁶. In DBSs, the excess electron is stabilised by the interaction with the molecule’s significant dipole moment. QBSs, on the other hand, arise from electrostatic interactions involving a large

quadrupole moment in molecules with no dipole moment. Unlike DBSs, no definitive critical quadrupole moment has been established for the formation of quadrupole-bound states¹². Lastly, CBSs are stabilised not by electrostatic forces but by dispersion interactions. It is worth noting that many DBSs and QBSs remain unbound if electron correlation effects are ignored, which blurs the distinction between these types of non-valence anions¹⁶. Examples of different anion types are shown in Figure 1.1.

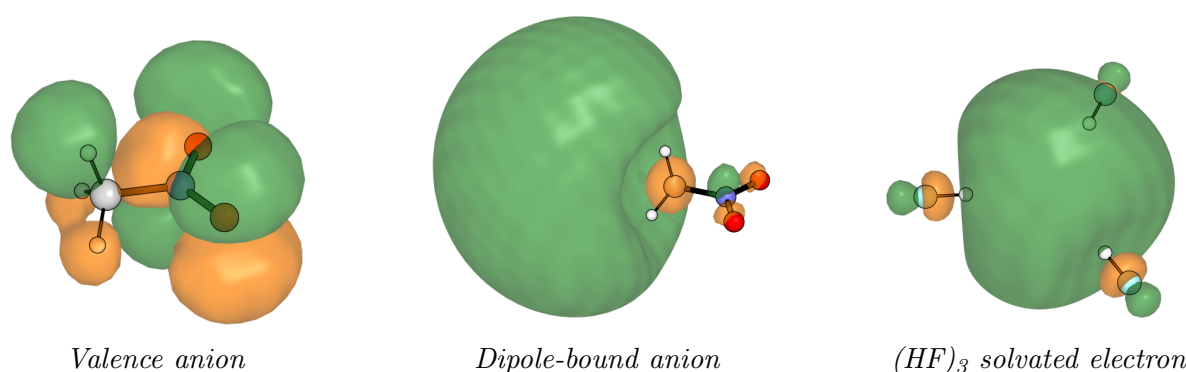


Figure 1.1: Dyson orbital for different types of anions: a) Valence bound state of nitromethane anion, b) dipole bound state of nitromethane, c) solvated electron by a HF trimer.

1.1.1 Dipole-Bound Anions

Of the different non-valence anions, DBSs are the most common and well-studied. They were first proposed in 1947, when it was demonstrated that an ideal dipole could bind an excess electron if the dipole moment exceeds 1.6 D⁵. Regarding ‘real’ molecules, it is now generally accepted that a dipole moment of approximately 2.5 D is required to bind an extra electron, although having a dipole moment above this threshold does not guarantee the formation of a dipole-bound anion.⁸

The weak forces that bind the excess electron are responsible for the diffuse nature of the state, with the electronic density often extending several Ångströms away from the nuclei, and their relatively low binding energy, usually below 0.1 eV. This makes them susceptible to external perturbations, such as solvent interactions or electric fields, which can significantly influence their stability and reactivity^{1,4,8,17–21}

DBSs poses binding energies comparable to thermal energy ($k_bT \sim 23$ meV), which might suggest limited practical relevance due to potential detachment. However DBSs can play a significant role in systems that support both VBSs and NVSs. These systems can undergo a transition from a non-valence anion state to a stable valence state^{4,8}. Moreover, since the electron density of an NVS is spatially extended and resides far from the nuclei, the relaxed structure of an NVS is much closer to that of the neutral molecule compared to a VBS. This large spatial extent also results in a higher cross-

section for electron capture and transfer. Consequently, DBSs can act as "doorway" states, facilitating electron capture and transfer processes^{1,2,8,22–28}. This unique behavior has sparked interest in the role of NVSs across various fields, including astrochemistry²⁹ and radiobiology^{30–32}.

1.1.2 Approaches to Study Non-Valence Anions

Significant progress has been made in experimental and theoretical methods for elucidating the structure and dynamics of NVSs.^{1,2,33} Experimentally, dipole-bound anions are characterised using spectroscopic techniques designed to probe their weakly bound electronic states^{34–36}. In photodetachment and photoelectron spectroscopies, a beam of the target species is generated—often using a laser vaporisation or electrospray source—and probed with light. The energy of the ejected electrons reveals information about the electron binding energy and electronic structure. Time-resolved photoelectron spectroscopy (TRPES)^{37,38} extends this approach, using ultrafast laser pulses to investigate the dynamics of electron attachment and detachment on femtosecond timescales, revealing transient states and relaxation pathways. DBSs can also be accessed by Rydberg electron transfer spectroscopy (RET)^{20,39,40}, which has been used to probe their role in electron transfer dynamics. Time-of-flight mass spectrometry is often coupled with these techniques to identify and isolate the correct anionic species^{6,41,42}.

The theoretical investigation of DBAs presents two main challenges. Firstly, the large spatial extent of the DB orbital requires atomic orbital basis sets that are sufficiently diffuse to accurately describe it, necessitating the use of large custom basis sets⁴³. Secondly, electron correlation is important; although the electron density at the valence level remains largely unchanged from the parent molecule, the diffuse part of the density, corresponding to the DB state, is considerably polarisable due to its diffuse nature and exhibits significant dispersion-like interactions with the valence region, contributing substantially to the binding energy of the extra electron^{1–3,7,16}.

Regarding computational methods, standard density functional theory (DFT) approaches can fail because most exchange-correlation functionals cannot properly describe dispersion interactions and can suffer from spin contamination in open-shell molecules⁴⁴. Multiconfigurational methods like complete active space self-consistent field (CASSCF)^{45,46} can capture the static correlation of the open shell systems, but require considerable effort in selecting an appropriate active space that balances accuracy and computational feasibility. Moreover, they lack dynamic correlation inherent in the dispersion. Currently, equation-of-motion coupled-cluster (EOM-CC)^{4,8,47} methods are often used for DBA modelling as they adequately treat both the electron correlation and open-shell character. However, the high computational cost of EOM-CC approaches significantly limits their

applicability to larger molecular systems. To address this, some approximate methods have been developed, such as the domain-based local pair natural orbital coupled-cluster theory (DLPNO) method^{48,49}, or the second order approximate CC2^{50,51}, which is used in this work.

1.1.3 Non-Valence Anions in Condensed Matter

Several studies have indicated that the presence of individual molecules interacting with a molecule supporting an NVS can further stabilise the state by increasing the total dipole moment, or by combining individual dipoles to collectively bind the electron in an intermolecular cavity. The excess electron is stabilised by the interaction with multiple solvent molecules, rather than binding to any individual molecule, and is known as a solvated electron^{1,4,8,17,19–21}

The binding energy of such solvated electrons can increase dramatically with cluster size. A water molecule does not support any bound anionic state⁴, however a water dimer anion $(\text{H}_2\text{O})_2^-$ exhibits low vertical detachment energy (VDE) of 45 meV⁵². Water cluster anions $(\text{H}_2\text{O})_n^-$ made of *ca.* 100 molecules can achieve VDEs exceeding 2.0 eV⁵³, and in bulk this value is measured to be higher than between 3.4 and 4 eV^{54,55}. The structure of the state was the subject of much debate in the literature^{56–59}, but it is now generally accepted that the excess electron resides in a cavity of approximately 2.5 Å in size⁵⁷. Solvent molecules can transform a weakly bound non-valence state into a strongly bound electronic species, though with significantly altered properties.

For solutes, the existence of hydrated NVSs still remains a subject of discussion^{60–62}. Computational studies suggest that hydration influences the localisation of the excess electron, often displacing it onto the surface of the solvent cage⁶⁰. Conversely, experimental evidence indicates that alkyl chains do not disrupt DBS stability⁶¹, and DBS-mediated mechanisms have been observed in solvated uracil systems⁶³. The viability of NVS in bulk systems depends on the molecular density and polarity of the medium. While solvents may hinder DBS existence due to excluded volume effects, they can also stabilise DBS through Van der Waals interactions^{40,64}. Distinct scenarios can be considered in the interaction between a DBA supporting molecule and solvent: the electron may be localised in the NVS orbital, captured by the solvent, or at the interface of the solute and solvent. The latter two phenomena are linked to charge-transfer-to-solvent (CTTS) electronic transitions and are observed experimentally^{40,64–66}.

1.1.4 Non-Valence Anions in Biological Systems

Research on dipole-bound anions (DBAs) has predominantly focused on gas-phase systems. However, in biological contexts, DBAs have garnered attention due to their inter-

actions with DNA, particularly in the context of radiation-induced damage and radiosensitizers^{30–32}. When high-energy radiation interacts with biological samples, it generates a cascade of secondary electrons which can be captured by cellular constituents, potentially through non-valence states. It has been hypothesised that NVSs in DNA act as electron scavengers, leading to strand breaks and other forms of damage^{25,30,31,63}. Radiosensitizers are drugs designed to enhance the efficacy of radiation therapy in cancer treatment. These compounds become cytotoxic upon capturing secondary electrons generated during radiation exposure, potentially through the formation of NVSs³².

The role of NVSs in natural biological pathways beyond genetic damage remains largely unexplored. It has been proposed that vacant pockets in proteins could accommodate non-valence states⁶¹. Enzymes play a crucial role in almost all biological reactions, particularly in the transfer and transport of electrons through biological matter. These processes are central to vital phenomena such as photosynthesis⁶⁷, aerobic respiration⁶⁸, and biological nitrogen fixation⁶⁹. The range of these electron transfers is remarkable, spanning timescales from picoseconds to milliseconds and distances between donor and final acceptor molecules from a few to over hundreds of Ångströms^{70,71}. Long-range electron transport is typically achieved through a chain of cofactors, often metal clusters, which facilitate a stepwise transfer of the electron. The inter-cluster distances range from a few Ångströms to over 20. As an example, in respiratory complex I, NADH donates electrons to reduce ubiquinone⁷². The binding sites of both molecules are around 110 Å apart, and the electron transfer is mediated by a series of cofactors. To model these transfer reactions, it is commonly assumed that the electron tunnels between the donor and acceptor. Specifically, in the superexchange model, the tunnelling process is mediated by unoccupied orbitals in the intervening space, effectively lowering the tunnelling barrier⁷¹. The sensitivity of non-valence anion states to environmental factors suggests a potential and elegant mechanism that natural systems could exploit to regulate long-range electron transfer processes.

In this study, we aim to focus on other biological targets, which could use an interplay between NVSs and VBSs. A natural compound with relevant roles in electron transfer in biological processes is ubiquinone.

1.2 Ubiquinone

Quinones, named for the bark of the cinchona tree from which they were isolated in the 18th century⁷⁵, are a class of organic compounds with a fully conjugated cyclic dione structure derived from aromatic compounds by conversion of an even number of C-H to ketone groups⁷⁶. Quinones are known for their redox properties and play crucial roles in various biological processes, including electron transport in cellular respiration and

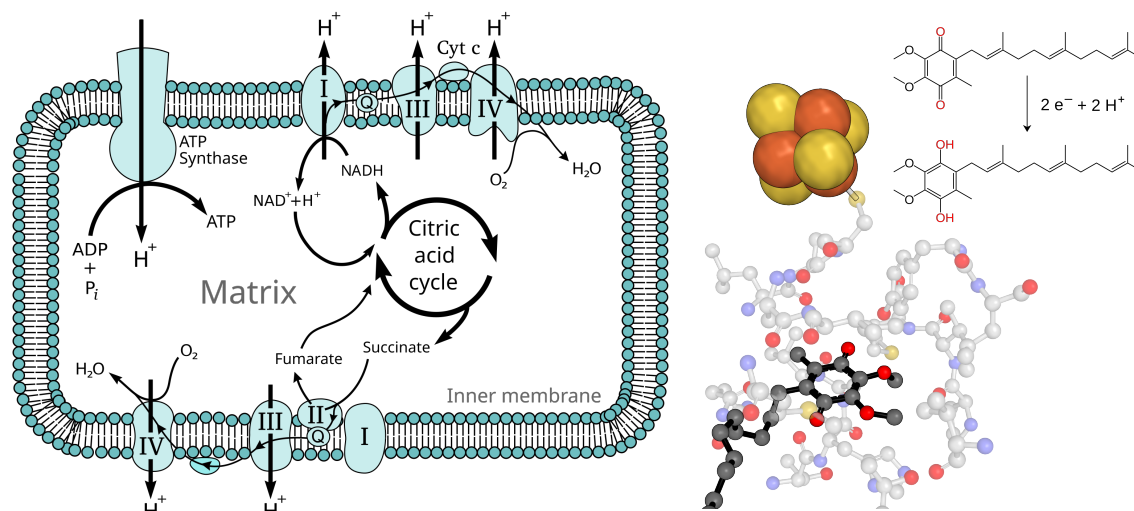


Figure 1.2: Roles of ubiquinone. Left; electron transport chain in the mitochondria, ubiquinones get reduced at complexes I and II and oxidized at complex III, adapted from 73. Right: CoQ at the active site of bacterial complex I (PDB: 6I0D)⁷⁴ and ubiquinone to ubiquinol interconversion.

photosynthesis^{72,77}.

This work focuses on ubiquinone -*ubi* from being ubiquitous in nature-, also known as coenzyme Q (CoQ), a lipid-soluble molecule that exists as a quinone or quinol, then named ubiquinol. It plays a role in aerobic respiration in the electron transport chain (ETC) as an electron carrier. As schematised in Figure 1.2, ubiquinone accepts 2 electrons at complexes I or II and donating them in complex III⁷².

Ubiquinone is composed of a benzoquinone ring, 2,3-dimethoxy-6-methyl-p-benzoquinone, and a long side chain, composed of a variable number of isoprenoid units depending on the organism, 10 in humans. This number, n , is used for the naming of the specific ubiquinone (Q_n). In Figure 1.3 different Q_n are presented. The benzoquinone moiety is responsible for its redox properties, while the isoprenoid tail enhances its lipid solubility, allowing it to integrate into biological membranes.⁷².

The ubiquinone moiety can support two types of anion states, a VBS and a DBA. In p-benzoquinone, the valence anion can be understood from the Hückel picture with the excess electron occupying a vacant π^* orbital. This state is stabilised relative to benzene due to the electron withdrawing ketone groups. In ubiquinone, the VBS is bound by around of 1.7 eV⁷⁷. The dipole-bound anion, on the other hand, results from the two methoxy chains, whose configuration mainly controls the dipole of the molecule⁴¹. It is a fairly rigid molecule, except for the dihedral angles between the methoxy groups and the benzoquinone ring and the isoprenoid tail. Their configuration will affect the dipole moment and could therefore determine the existence and energetics of the DBA^{41,78}. Therefore, fairly complicated electronic structure can be studied in terms of two coordinates.

When the isoprenoid tail is considered, it has been shown that it further stabilises the

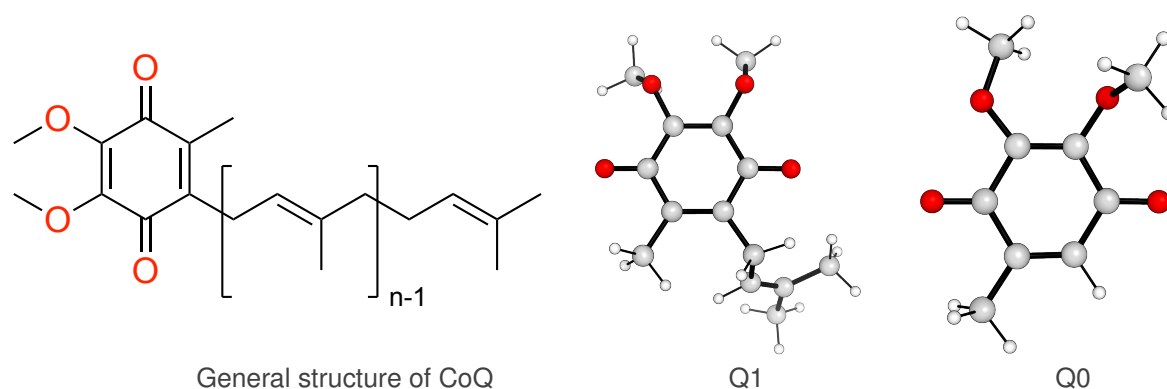


Figure 1.3: Quinones used in this work. From left to right: General structure of CoQ (or Q_n), Q₁, Q₀.

valence anion⁴². Its effects on the dipole state have not been studied. One can imagine the effect to be moderate for shorter tails; it will slightly modify the dipole moment of the system, but structurally will be quite far from the excess electron density. For longer tails, the isoprenoid chain could sterically hinder the dipole-bound state.

There have been extensive studies on the electron binding properties of the ubiquinone family, both experimentally^{41,42,78,79} and theoretically^{41,42,48,80,81}. However, these studies have focused on the valence anion of the quinone, and no comprehensive study of the dipole bound state has been performed. The VBS is the final acceptor of the electron and the existence of the DBA in condensed phase is dubious. However, experimental studies have observed dipole-bound anions in the gas phase in ubiquinones Q₀ and Q₁ with an EA of ~ 60 meV⁴¹. Although its signal is reduced as more isoprenoid units are added, interpreted as an effect of the isoprenoid tail being flexible and resulting in a steric hindrance of the state^{41,42}, one could imagine that in a protein moiety, the geometry of the tail would be fixed far from a potential DB orbital, which could even be further stabilised by residues pointing in the cavity. This motivates the current study.

1.3 Research Goals

The main objective of this work is to study the dipole-bound anion of ubiquinone. The electron attachment variant of equation-of-motion CC2 (EA-EOM-CC2) is used, which has recently shown to be effective in dipole bound states of organic molecules⁵¹. The specific objectives are:

- Benchmark the effectiveness of the EA-EOM-CC2 method to compute the electron affinity of quinones.
- Implement the Dyson orbital approach for EOM-CC2, for characterisation of elec-

tronic states of large systems beyond their energies.

- To investigate the dipole-bound anion of ubiquinone in terms of its functional group configurations.
- To study the effect of the molecular environment on the dipole-bound anion of ubiquinone, treated as a cluster model using small molecules.

Chapter 2

Theoretical Background

2.1 Self-Consistent Field Methods

Electronic structure theory aims to solve the time-independent Schrödinger equation (TISE) for a many-electron system, which governs the behavior of electrons within atoms and molecules:

$$\hat{H}\Psi = E\Psi \quad (1)$$

However, solving the TISE exactly for systems with more than one electron is computationally unfeasible due to its many body nature. To address this, approximate methods such as the Hartree-Fock (HF) method have been developed^{82,83}.

The Hartree-Fock (HF) method stands as the cornerstone electronic structure calculations⁸⁴. The HF method provides an approximate solution to the TISE within the Born-Openheimer approximation by assuming that each electron moves independently within an average electrostatic field generated by the other electrons in the system and nuclei. In the HF method the N -electron wavefunction is represented by a Slater determinant, which is formed by taking the antisymmetrized product of N individual one-electron spin-orbitals (χ):

$$\Psi(\mathbf{r}_1, \mathbf{r}_2, \dots, \mathbf{r}_N) = \frac{1}{\sqrt{N!}} \begin{vmatrix} \chi_1(\mathbf{r}_1) & \chi_2(\mathbf{r}_1) & \cdots & \chi_N(\mathbf{r}_1) \\ \chi_1(\mathbf{r}_2) & \chi_2(\mathbf{r}_2) & \cdots & \chi_N(\mathbf{r}_2) \\ \vdots & \vdots & \ddots & \vdots \\ \chi_1(\mathbf{r}_N) & \chi_2(\mathbf{r}_N) & \cdots & \chi_N(\mathbf{r}_N) \end{vmatrix} \quad (2)$$

The choice of using a determinant inherently satisfies the antisymmetry requirement of fermions. The Hartree-Fock equations are inherently non-linear: because the Fock operator depends on the wavefunctions of all the other electrons, their interactions are coupled. Consequently, these equations cannot be solved analytically and are solved using an it-

erative procedure known as the self-consistent field (SCF) method, where the final field experienced by the electrons must be consistent with the electron distribution that generates that field. Due to the two electron repulsion and exchange contributions, HF scales as $\mathcal{O}(N^4)$ in terms of computational cost, where N is the number of spinorbitals in the system. In practical Hartree-Fock calculations, the spinorbitals are expressed as linear combinations of predefined mathematical functions known as basis functions. The set of these functions is called a basis set. Because a finite basis set cannot exactly represent the spinorbitals, they define the level of accuracy and computational cost of the calculation. Larger basis sets generally lead to more accurate descriptions of the electronic structure at the cost of increased computational effort.

2.1.1 Electron Correlation

The Hartree-Fock (HF) method is inherently limited by its neglect of the instantaneous interactions of electrons. In the HF approximation, each electron is treated as moving independently within a static, average field created by the other electrons. This mean-field approach fails to account for the fact that electrons will instantaneously repel each other, leading to a correlated movement as they try to avoid each other in space.

The primary consequence of neglecting electron correlation in the HF approximation is an overestimation of the electron-electron repulsion energy, known as Coulomb, or dynamic, correlation. Due to this, the HF electronic energy is higher than the exact energy, and HF wavefunctions fail to capture certain phenomena, such as London dispersion forces. Correlated methods aim to include the effects of the instantaneous interactions between electrons that are neglected in the mean-field approximation of HF theory. In the following sections, several correlated methods relevant to this work are presented.

2.1.2 Møller-Plesset Perturbation Theory

Møller-Plesset (MP)⁸⁵ perturbation theory offers a way to improve upon the HF energy by the use of Rayleigh-Schrodinger perturbation theory: the electron correlation is treated as a perturbation to the HF Hamiltonian. The energy and wavefunction are then expanded as a series in terms of the perturbation strength. The first-order energy correction in MP theory is zero, so the first non-trivial correction to the HF energy appears at the second order, giving rise to the MP2 method. The MP2 energy correction for a closed-shell molecule is given by:

$$E_{\text{MP2}} = -\frac{1}{4} \sum_{ij}^{\text{occ}} \sum_{ab}^{\text{virt}} \frac{|\langle ij || ab \rangle|^2}{\epsilon_a + \epsilon_b - \epsilon_i - \epsilon_j} \quad (3)$$

Where i, j denote occupied molecular orbitals, a, b denote virtual molecular orbitals, and ϵ are the corresponding orbital energies from the HF calculation. MP theory can be extended to higher orders (MP3, MP4, etc.) to achieve greater accuracy, although the computational cost increases significantly with each order. The computational cost of MP2 scales as $\mathcal{O}(N^5)$.

2.1.3 Density Functional Theory

Density functional theory (DFT)^{86,87} provides an alternative approach to incorporating electron correlation by parametrizing the energy on the electron density rather than the wavefunction, reducing the degrees of freedom of the system from $3N - 3$ to just 3, where N is the number of electrons. In the most commonly used form of DFT, the Kohn-Sham method, the problem is formulated terms of orbitals that are not physical, but are chosen to reproduce the electron density of the system. The fundamental principle of DFT is that the ground state energy of a system is a unique functional of its electron density:

$$\left(-\frac{1}{2}\nabla^2 + \hat{V}_{\text{ext}}(\mathbf{r}) + \hat{V}_{\text{H}}(\mathbf{r}) + \hat{V}_{\text{XC}}[\rho(\mathbf{r})] \right) \psi_i(\mathbf{r}) = \epsilon_i \psi_i(\mathbf{r}) \quad (4)$$

Where \hat{V}_{ext} represents the external potential, $\hat{V}_{\text{H}}(\mathbf{r}) = \int \frac{\rho(\mathbf{r}')}{|\mathbf{r}-\mathbf{r}'|} d\mathbf{r}'$ is the Hartree potential, \hat{V}_{XC} is the exchange-correlation potential and $\rho(\mathbf{r})$ is the electron density. The exchange-correlation functional is not known exactly and must be approximated, and the accuracy of DFT calculations depends heavily on the its choice. The computational cost of DFT scales as $\mathcal{O}(N^4)$.

2.1.4 Configuration Interaction

Configuration Interaction (CI)^{85,88} methods improve upon HF by expressing the electronic wavefunction as a linear combination of the HF ground state determinant and excited state determinants:

$$|\Psi_{\text{CI}}\rangle = c_0|\Phi_0\rangle + \sum_{ia} c_{ia}|\Phi_{ia}\rangle + \sum_{ijab} c_{ijab}|\Phi_{ijab}\rangle + \dots \quad (5)$$

Where $|\Phi_0\rangle$ is the HF ground state determinant, $|\Phi_{ia}\rangle$ represents a determinant with a hole in spin-orbital i and a particle in the spin-orbital a , and c are the CI coefficients. Full CI (FCI), includes all possible excitations within a given one-electron basis set and represents the exact solution to the non-relativistic Schrödinger equation in that basis. However, is computationally prohibitive for all but the simplest systems. Full Configuration Interaction (FCI) includes all possible excitations within a given one-electron basis set and represents the exact solution to the non-relativistic Schrödinger equation in that

basis. However, it is computationally prohibitive for all but the simplest systems and in practice CI methods are always truncated.

A method is size-extensive if, for two infinitely separated molecules A and B , the total energy satisfies $E(A + B) = E(A) + E(B)$. Truncated CI methods, such as CISD (singles and doubles), are more practical but lack size extensivity. CI are, however, size-consistent, meaning that the energy behaviour remains consistent when interaction between the involved molecular subsystems is nullified (by distance, for instance). While CISD is size-consistent, its lack of size extensivity makes it unsuitable for extensive systems.

2.1.5 Coupled Cluster Theory

Similarly to CI, the coupled cluster (CC)^{85,89–92} method expands the wavefunction as a linear combination of Slater determinants. However, the CC wavefunction is size-extensive and size-consistent by using an exponential ansatz,

$$|\Psi_{\text{CC}}\rangle = e^{\hat{T}}|\Psi_0\rangle \quad (6)$$

where \hat{T} is the cluster operator, which is the central component of CC theory and is defined as a sum of excitation operators,

$$\hat{T} = \hat{T}_1 + \hat{T}_2 + \hat{T}_3 + \cdots + \hat{T}_N \quad (7)$$

where N is the total number of electrons in the system. Each term in this sum corresponds to a specific level of excitation and is expressed within the second quantization formalism as:

- $\hat{T}_1 = \sum_i^{\text{occ}} \sum_a^{\text{virt}} t_i^a a_a^\dagger a_i$ represents single excitations.
- $\hat{T}_2 = \frac{1}{4} \sum_{i,j}^{\text{occ}} \sum_{a,b}^{\text{virt}} t_{ij}^{ab} a_a^\dagger a_b^\dagger a_j a_i$ represents double, *coupled* excitations.
- Higher-order excitation operators $\hat{T}_3, \hat{T}_4, \dots$ describe coupled excitation of three, four, and more electrons, respectively.

The coefficients t_i^a , t_{ij}^{ab} , etc., are cluster amplitudes determined by projection of the CC Schrödinger equation onto the excited determinant. The exponential form, expanded as a Taylor series,

$$e^{\hat{T}} = 1 + \hat{T} + \frac{1}{2!}\hat{T}^2 + \dots \quad (8)$$

inherently includes terms that represent disconnected clusters, which ensures size consistency. The energy is obtained by projecting onto the HF reference determinant:

$$E_{CC} = \langle \Psi_0 | e^{-\hat{T}} \hat{H} e^{\hat{T}} | \Psi_0 \rangle \quad (9)$$

It can be shown that the exponential operators in Eq. 9 can be simplified to a series of commutators which ends at the fourth order. The cluster operator \hat{T} can be truncated at different levels of excitation:

- **CCD** (Coupled Cluster Doubles): This is the simplest approximation in the CC family, where the cluster operator is truncated to include only double excitations: $\hat{T} \approx \hat{T}_2$. There is no CC Singles since Brillouin's theorem implies that the amplitudes of single excitations alone are null.
- **CCSD** (Coupled Cluster Singles and Doubles): This is one of the most widely used and generally accurate *ab initio* methods, where the cluster operator includes both single and double excitations: $\hat{T} \approx \hat{T}_1 + \hat{T}_2$.
- **CCSDT** (Coupled Cluster Singles, Doubles, and Triples): $\hat{T} \approx \hat{T}_1 + \hat{T}_2 + \hat{T}_3$.
- ...

The hierarchy can be extended to include even higher levels of excitation, with the properties converging to the FCI limit. The computational cost of CC methods increases rapidly with the level of truncation, as shown in Table 2.1.

Because of the truncation of the excitation operators, the similarity-transformed Hamiltonian becomes non-Hermitian, leading to distinct left and right eigenfunctions for the same eigenvalue that form a biorthonormal set, satisfying $\langle \Psi_i^L | \Psi_j^R \rangle = \delta_{ij}$. While the right eigenfunction is parametrised as $|\Psi_{CC}\rangle = e^{\hat{T}}|\Phi_0\rangle$, the left eigenfunction is expressed as $\langle \Psi_{CC}^L| = \langle \Phi_0|(1 + \hat{\Lambda})e^{-\hat{T}}$, where $\hat{\Lambda}$ is the de-excitation operator:

$$\hat{\Lambda} = \hat{\Lambda}_1 + \hat{\Lambda}_2 + \dots = \sum_i^{\text{occ}} \sum_a^{\text{virt}} \lambda_i^a a_i^\dagger a_a + \frac{1}{4} \sum_{ij}^{\text{occ}} \sum_{ab}^{\text{virt}} \lambda_{ij}^{ab} a_i^\dagger a_j^\dagger a_b a_a + \dots \quad (10)$$

and λ the amplitudes to be determined. The biorthogonal formulation is essential for calculating transition properties, like the transition dipole moment, non-adiabatic coupling, and Dyson orbitals.

2.1.6 Second Approximate Coupled Cluster

Second approximate coupled cluster (CC2)⁸⁵ belongs to the broader family of CCn approximate coupled cluster methods, where the 'n' in CCn indicates the truncation of the

cluster operator within a perturbative hierarchy. These methods aim to reduce the computational cost associated with standard CC truncations while still retaining a reasonable level of accuracy.

In CC2, the equations for the single amplitudes, t_i^a , are the same as CC theory (Eq. 6) under the constraint that the doubles amplitudes, t_{ij}^{ab} , are calculated using the non-iterative expression for MP2 (Eq 3). The resulting expression for the CC2 correlation energy is:

$$E_{\text{CC2}} = \frac{1}{4} \sum_{ij}^{\text{occ}} \sum_{ab}^{\text{virt}} \frac{|\langle ab || ij \rangle|^2}{\epsilon_a + \epsilon_b - \epsilon_i - \epsilon_j} + \sum_i^{\text{occ}} \sum_a^{\text{virt}} \hat{F}_{ai} t_i^a \quad (11)$$

The perturbative treatment of the doubles amplitudes in CC2, reduces the computational cost compared to CCSD, Table 2.1. While this approximation can lead to a less accurate description of electron correlation, the inclusion of singles amplitudes allows for an approximate description of orbital relaxation, which often leads to higher quality wavefunction, and hence properties, compared to MP2. Additionally, the memory scaling can be reduced from N^4 to N^3 by using the resolution-of-the-identity (RI) approximation or Cholesky decomposition to the two electron integrals, which are approximated using an auxiliary basis set, effectively reducing them from a product of four-index to three-index quantities.⁹³

Table 2.1: Computational scaling of quantum chemistry methods, canonical memory usage is indicated as Memory, whereas RI memory usage is indicated as RI Memory. The operation count is given in terms of the number of spin-orbitals, N .

Method	Operation count	Memory	RI Memory
HF	$\mathcal{O}(N^4)$	$\mathcal{O}(N^4)$	$\mathcal{O}(N^3)$
KS DFT	$\mathcal{O}(N^4)$	$\mathcal{O}(N^4)$	$\mathcal{O}(N^3)$
CCD/CCSD	$\mathcal{O}(N^6)$	$\mathcal{O}(N^4)$	$\mathcal{O}(N^4)$
CCSDT	$\mathcal{O}(N^8)$	$\mathcal{O}(N^6)$	$\mathcal{O}(N^6)$
CC2	$\mathcal{O}(N^5)$	$\mathcal{O}(N^4)$	$\mathcal{O}(N^3)$

2.2 Equation-of-Motion Methods

Equation-of-motion coupled cluster (EOM-CC) methods^{94–96} are an extension of ground-state coupled cluster theory to excited (EE), ionized (IP) and electron-attached (EA) states. In the EOM-CC, the target electronic state is generated by applying a linear excitation operator \hat{R} to a reference state, which typically is the coupled cluster wavefunction of the ground state. The target state wavefunction can then be expressed as $|\Psi_{\text{EOM}}\rangle = \hat{R}|\Psi_{\text{CC}}\rangle = \hat{R}e^{\hat{T}}|\Phi_0\rangle$. Figure 2.1, shows some of the determinants of $|\Psi_{\text{EA}}\rangle$, where

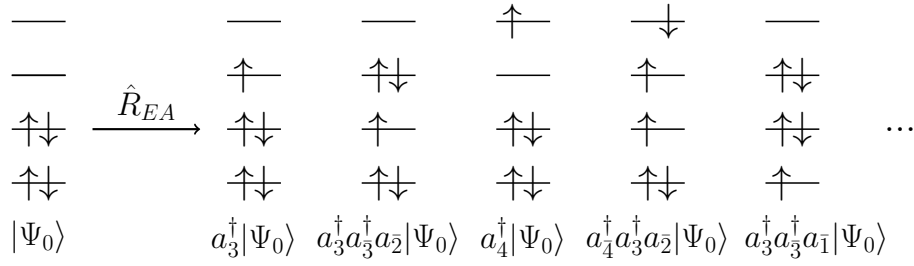


Figure 2.1: Schematic representation of the EOM-EA method. The target state is generated by applying the electron attachment operator \hat{R}^{EA} to the reference state. The resulting wavefunction contains contributions from various determinants with one more α electron.

the target state has one more α -spin electron.

The form of the operator \hat{R} is similar to the cluster operator and chosen to access the desired target state. In the case of EOM-EA, the electron attachment operator R^{EA} includes terms that describe the creation of one electron in an unoccupied orbital, terms that describe the creation of one electron accompanied by the excitation of another electron:

$$\hat{R}^{\text{EA}} = \hat{R}_1^{\text{EA}} + \hat{R}_2^{\text{EA}} + \dots = \sum_a r^a a_a^\dagger + \frac{1}{2} \sum_{ab} \sum_i r_i^{ab} a_a^\dagger a_b^\dagger a_i + \dots \quad (12)$$

where a and b denote virtual orbitals, i denotes an occupied orbital, and r^a and r_i^{ab} are the coefficients to be determined. By truncating at the same excitation level as the cluster operator, the method is rigorously size-extensive and size-consistent. The EA energies, or any other EOM energy, can be obtained as the eigenvalues of the similarity-transformed Hamiltonian, \bar{H}_N :

$$\bar{H}_N \hat{R} |\Psi_0\rangle = \Delta E_{\text{EOM}} \hat{R} |\Psi_0\rangle \quad (13)$$

$$\bar{H}_N = e^{-\hat{T}} \hat{H} e^{\hat{T}} - \langle \Psi_0 | e^{-\hat{T}} \hat{H} e^{\hat{T}} | \Psi_0 \rangle \quad (14)$$

As in coupled cluster, the similarity transformed Hamiltonian is non-Hermitian and left and right eigenvectors are different but correspond to the same eigenvalues. This means that the properties have ‘right’ and ‘left’ expectation values. The left deexcitation operator \hat{L} , analogous to \hat{R} for the left eigenstates, takes the following form for EOM-EA:

$$\hat{L}^{\text{EA}} = \hat{L}_1^{\text{EA}} + \hat{L}_2^{\text{EA}} + \dots = \sum_a l^a a_a + \frac{1}{2} \sum_{ab} \sum_i l_i^{ab} a_i^\dagger a_b a_a + \dots \quad (15)$$

Where l^a and l_i^{ba} are the amplitudes to be determined. And the ‘left’ wavefunction is $\langle \Psi_{\text{EOM}} | = \langle \Psi_{\text{CC}} | \hat{L} = \langle \Phi_0 | (1 + \hat{\Lambda}) e^{-\hat{T}} \hat{L}$.

One strength of the EOM-CC ansatz is the use of a closed shell reference to access open

shell states, which are eigenfunctions of the \hat{S}^2 operator. Finally, the computational cost of EOM-CC methods is similar to that of the corresponding ground-state CC method.

2.3 Dyson Orbitals

Dyson orbitals^{97,98} are defined as the overlap between the wavefunction of an initial N -electron state ($|\Psi_0^N\rangle$) and the wavefunction of the final state with $N\pm 1$ electrons ($|\Psi_f^{N\pm 1}\rangle$).

$$\phi_d(r_1) = \sqrt{N} \int \Psi^N(r_1, \dots, r_{N-1}) \Psi^{N+1}(r_1, r_2, \dots, r_N) dr_1 \dots dr_{N-1} \quad (16)$$

Because the terms differ in one electron, the result of the overlap is a vector instead of a scalar, and can be expressed as a linear combination of the molecular orbitals ($\phi_p(r)$) of the reference wavefunction:

$$\phi_d(r) = \sum_p \gamma_p \phi_p(r) \quad (17)$$

where γ_p are the coefficients that quantify the contribution of each molecular orbital to the Dyson orbital. Physically, Dyson orbitals can be interpreted as the correlated analogue to the orbital of the electron that is either removed or attached.

The norm squared of the Dyson orbital, P , is calculated by integrating the squared modulus of the Dyson orbital over all space:

$$P = \int |\phi_d(r)|^2 dr = \sum_{p,q} \gamma_p^* \gamma_q \langle \phi_p | \phi_q \rangle \quad (18)$$

It ranges from 0 to 1 and provides a direct measure of the one-electron character of the ionization or electron attachment process. If the open shell wavefunction is obtained by means of an EOM-CC method, there is a ‘left’ and a ‘right’ Dyson orbital. By convention, the right Dyson orbital is obtained when the Ψ^{N+1} is in the bra and the Ψ^N is in the ket.

On top of providing a visual representation of the transition process, they can be used for the interpretation and prediction of photoelectron spectra as they contain all the information required to calculate differential cross-sections, $\frac{d\sigma}{d\Omega_k}$:

$$\frac{d\sigma}{d\Omega_k} = \frac{4\pi^2 k E}{c} |\langle \phi_d | \mu | \Psi_k^{el} \rangle|^2 \quad (19)$$

where k is the magnitude of the photoelectron wavevector, E is the energy of the ionizing radiation, and c is the speed of light, μ is the dipole operator, and Ψ_k^{el} is the photoelectron wavefunction, and a strong orthonormality is assumed between the reference and continuum wavefunction.

2.3.1 EOM-CC2 Dyson Orbital Equations

The algebraic expressions for the EOM-CC2 Dyson orbitals are identical to the CCSD ones. A derivation of the algebraic expression of Dyson orbitals in terms of the t , r , l , λ amplitudes is presented for the EA-EOM case, and the expression for the other EOM flavours implemented in this work follow. It is important to realize that the operators involved (\hat{T} , $\hat{\Lambda}$, \hat{R} , \hat{L}) affect the occupation of the spin-orbitals, and thus only the combinations of terms which leave the reference wavefunction, $|0\rangle$, unchanged survive. To find these combinations, commutators can be used to reorder the operators involved.

EOM-EA-CC Dyson Equations

In the case of the right EOM-EA-CC Dyson orbital amplitudes:

$$\gamma_i^{\text{EA,R}} = \langle EA | \hat{a}_i^\dagger | CC \rangle = \langle 0 | \hat{L}^{EA} e^{-\hat{T}} \hat{a}_i^\dagger e^{\hat{T}} | 0 \rangle$$

The following equalities are useful:

$$e^{-\hat{T}} e^{\hat{T}} = e^{\hat{T}} e^{-\hat{T}} = 1$$

$$[e^{\pm\hat{T}}, \hat{a}_p^\dagger] = [\cancel{1, \hat{p}^\dagger}] \overset{0}{\nearrow} \pm t_j^b [\hat{b}^\dagger \hat{j}, \hat{p}^\dagger] \pm t_{jk}^{bc} [\hat{b}^\dagger \hat{c}^\dagger \hat{k} \hat{j}, \hat{p}^\dagger] + \dots$$

Where a change of notation, $a_p^\dagger \rightarrow p^\dagger$, upon expansion is done for readability. Two cases are distinguished, p is a virtual orbital, a , or an occupied orbital, i . For virtual orbitals, $p = a$:

$$[\hat{b}^\dagger \hat{j}, \hat{a}^\dagger] = \hat{b}^\dagger \hat{j} \hat{a}^\dagger - \hat{a}^\dagger \hat{b}^\dagger \hat{j} = (-1)^2 \hat{a}^\dagger \hat{b}^\dagger \hat{j} - \hat{a}^\dagger \hat{b}^\dagger \hat{j} = 0$$

Similarly with higher order terms, it is arrived to:

$$[e^{\pm\hat{T}}, \hat{a}_a^\dagger] = 0$$

For occupied orbitals, $p = i$:

$$[\hat{b}^\dagger \hat{j}, \hat{i}^\dagger] = \hat{b}^\dagger \hat{j} \hat{i}^\dagger \overset{0}{\nearrow} - \hat{i}^\dagger \hat{b}^\dagger \hat{j}$$

And similarly with higher order terms:

$$[e^{\pm\hat{T}}, \hat{a}_i^\dagger] = -\hat{a}_i^\dagger (e^{\pm\hat{T}} - 1)$$

These relations can now be used to derive the expression for the occupied and virtual Right EOM-EA-CC Dyson orbital amplitudes:

$$\phi_D^{\text{EA,R}} = \sum_p \gamma_p^{\text{EA,R}} \phi_p = \sum_i^{\text{occ}} \gamma_i^{\text{EA,R}} \phi_i + \sum_a^{\text{vir}} \gamma_a^{\text{EA,R}} \phi_a$$

The general expression can be reordered:

$$\begin{aligned} \gamma_p^{\text{EA,R}} &= \langle EA | \hat{a}_p^\dagger | CC \rangle = \langle 0 | \hat{L}^{EA} e^{-\hat{T}} \hat{a}_p^\dagger e^{\hat{T}} | 0 \rangle \\ &= \langle 0 | \hat{L}^{EA} (\hat{a}_p^\dagger e^{-\hat{T}} + [e^{-\hat{T}}, \hat{a}_p^\dagger]) e^{\hat{T}} | 0 \rangle \end{aligned} \quad (20)$$

For virtual orbitals, $p = a$:

$$\begin{aligned} \gamma_a^{\text{EA,R}} &= \langle 0 | \hat{L}^{EA} (\hat{a}_a^\dagger e^{-\hat{T}} + [e^{-\hat{T}}, \hat{a}_a^\dagger]) e^{\hat{T}} | 0 \rangle \\ &= \langle 0 | \hat{L}^{EA} \hat{a}_a^\dagger e^{-\hat{T}} e^{\hat{T}} | 0 \rangle = \langle 0 | \hat{L}^{EA} \hat{a}_a^\dagger | 0 \rangle \\ &= \langle 0 | l_a \hat{a} \hat{a}^\dagger | 0 \rangle \\ &= l_a \end{aligned} \quad (21)$$

For occupied orbitals, $p = i$:

$$\begin{aligned} \gamma_i^{\text{EA,R}} &= \langle 0 | \hat{L}^{EA} (\hat{a}_i^\dagger e^{-\hat{T}} + [e^{-\hat{T}}, \hat{a}_i^\dagger]) e^{\hat{T}} | 0 \rangle \\ &= \langle 0 | \hat{L}^{EA} (\hat{a}_i^\dagger e^{-\hat{T}} - \hat{a}_i^\dagger e^{-\hat{T}} + \hat{a}^\dagger) e^{\hat{T}} | 0 \rangle = \langle 0 | \hat{L}^{EA} \hat{a}_i^\dagger e^{\hat{T}} | 0 \rangle \\ &= \langle 0 | l_b t_i^b \hat{b} \hat{i}^\dagger \hat{b}^\dagger \hat{i} + l_{bc}^j t_{ij}^{bc} \hat{b} \hat{c} \hat{j}^\dagger \hat{i}^\dagger \hat{b}^\dagger \hat{c}^\dagger \hat{i} \hat{j} | 0 \rangle \\ &= - \sum_c t_{ic} l_c - \frac{1}{2} \sum_{kcd} t_{ki}^{dc} l_{dc}^k \end{aligned} \quad (22)$$

A similar approach can be applied to the other Dyson equations to obtain their corresponding expressions, which can be found in appendix A.

Chapter 3

Computational Details

TODO: complete and divide in subsection

All electronic structure calculations were performed using the developer’s copy of the *Q-Chem* software⁹⁹. In all computations the frozen-core approximation is used, only the valence electrons are correlated, as well as the resolution of the identity (RI) approximation, auxiliary basis functions are used to approximate the two-electron integrals⁹³.

For the EOM-EA calculations, the reference wavefunction was obtained as the restricted Hartree-Fock (RHF) solution of the ground state of the neutral molecule. Unless explicitly mentioned, calculations were performed at using the aug-cc-pVDZ basis set¹⁰⁰ further augmented by 3 s-shells on hydrogen atoms and 6 s- and 3 p-shells on all non-hydrogen atoms⁵¹ to properly model the non-valence states. The coefficients of the extra functions were obtained by successively halving the most diffuse function of the original set..

CC2 Dyson orbitals for EOM variants described in section 2.3.1 and appendix A were implemented as described, and will be released in an upcoming version of *Q-Chem*.

All closed-shell quinone model geometries were optimized using the TPSS functional¹⁰¹ with Grimme’s pair-wise dispersion corrections with Becke-Johnson damping (D3BJ)¹⁰², and the minimally augmented¹⁰³ def2-TZVP basis sets¹⁰⁴ (ma-def2-TZVP), following the work in⁴⁹. For the scan calculations, each single point was optimized constraining its relevant angles by the method of Lagrange multipliers; dihedrals of the methoxy chains of Q0 and Q1, and the isoprene tail of Q1. In the case of quinone + aminoacid models, crystal structures were taken from the Protein Data Bank (PDB). Hydrogens were added using *PyMOL*’s¹⁰⁵ `add_H` functionality, and relaxed using the method above (fixing the rest of the heavy atoms).

For the scans of quinone + molecule, each subsystem was independently optimized and put together with any further refinement.

For quinone systems, only EOM-EA right Dyson orbitals were computed to speed up the calculations by avoiding the need to compute the lambda terms.

Photoionization and Photodetachment cross-sections were calculated using the *ezDyson* package^{106,107}.

Chapter 4

Results and Discussion

4.1 Performance of EOM-CC2 Related Methods

4.1.1 Basis Set Dependence of EA-EOM-CC2 in Dipole Bound Anions

The basis set dependence of EA-EOM-CC2 for dipole-bound radical anions was evaluated using a test set of 14 DBS of organic taking as reference EA-EOM-CCSD⁵¹. The results as summarised in Table 4.1. The binding energies ranging from less than 1 meV for acetone to approximately 26 meV for nitrobenzene. The table also show how the binding energy does not correlate strongly with the magnitude of the dipole moment for different species. For instance, phenylisocyanide, which has a slightly lower dipole moment than benzaldehyde, exhibits an electron affinity nearly twice as large.

The basis set cardinality was varied from DZ to QZ for EA-EOM-CC2 and from DZ to TZ for CCSD, while keeping additional diffuse functions fixed at 6s3p for heavy atoms and 3s for hydrogens, referred to as (6s3p). For the EA-EOM-CC2 method, the influence of diffuse functions was further explored by fixing the cardinality to TZ and incrementally increasing the number of diffuse functions from 2s1p for heavy atoms and 1s for hydrogens, referred to as (2s1p), to 8s4p for heavy atoms and 4s for hydrogens, referred to as (8s4p). The coefficients of the diffuse functions are detailed in the methods' section 3. For comparison, the dipole strength, calculated at the HF level, and Koopmans' theorem (KT), which estimates the binding energy using the energy of the lowest unoccupied molecular orbital, are also included.

Starting with the simplest approximation, KT predicts that all anions with an EOM-EA-CCSD binding energy below 10 meV become unbound. However, even for more strongly bound cases, Koopmans' theorem significantly underestimates the binding energy, capturing only 20% of the binding energy for nitrobenzene, for example.

No DBS is predicted when only the 2s1p diffuse function are added. At the 6s3p level the DBS energy is converged with respect to the extra diffuse functions added to the basis set, deviating by less than 1 meV from the value obtained with the 8s4p diffuse function. The errors are more pronounced for smaller molecules, such as acetaldehyde and acetone. This could be attributed to the inability of functions centred on a few atoms to adequately cover the spatial extent of the DBS orbital. This reasoning may also explain why the DBS of acetaldehyde is only predicted by RI-EA-EOM-CC2/aug-cc-pVTZ+8s4p, as it employs the most diffuse functions.

The binding energy increases with higher cardinality, as expected, due to the increased flexibility of the basis set. However, this effect is less significant than the addition of diffuse functions. For instance, the difference between RI-EA-EOM-CCSD/aug-cc-pVDZ+6s3p and RI-EA-EOM-CCSD/aug-cc-pVTZ+6s3p is less than 1 meV for most cases. Smaller molecules with lower-energy DBSs tend to be more challenging; for example, a TZ basis is required to predict the DBS of acetone. In general, and especially for larger systems, the inclusion of diffuse functions is more critical than the cardinality of the basis set for dipole-bound anions.

CC2/aug-cc-pVTZ+6s3p consistently overestimates the binding energies across all molecules when compared to CCSD/aug-cc-pVTZ+6s3p. The mean absolute error (MAE) is 2 meV, with deviations reaching up to 10 meV for nitrobenzene. For this reason, using a smaller cardinality results in a cancellation of errors for CC2. The aug-cc-pVDZ+6s3p basis set, when employed with CC2, yields the lowest MAE of 2.3 meV compared to the reference RI-EA-EOM-CCSD/aug-cc-pVTZ+6s3p results.

Table 4.1: Electron affinity of dipole-bound radical anions computed using different augmented Dunning basis sets and EOM-EA RI-CC2 and RI-CCSD⁵¹. Koopman’ theorem (KT), and dipole moment, μ , calculated at the HF/aug-cc-pVTZ+6s3p level, and mean absolute error (MAE) are also given. The values are in meV and Debye respectively.

Molecule		RI-CC2						RI-CCSD		KT	μ
		aug-cc-pVTZ				pVDZ	pVQZ	pVDZ	pVDZ		
		2s1p	4s2p	6s3p	8s4p	6s3p	6s3p	6s3p	6s3p		
Acetaldehyde	CH ₃ CHO	-156.7	-27.8	-3.2	0.8	-4.6	-3.2	-4.6	-3.1	-0.4	3.29
Acetone	(CH ₃) ₂ CO	-114.9	-16.8	1.3	3.3	-0.3	0.9	-0.5	0.9	-5.1	3.46
Acetonitrile	CH ₃ CN	-61.2	12.6	19.9	20.1	18.2	20.3	17.1	18.4	4.2	4.29
Benzaldehyde	C ₆ H ₅ CHO	-97.1	-2.1	8.9	9.6	7.4	9.1	3.4	4.6	-4.9	3.77
N,N-Dimethylformamide	(CH ₃) ₂ NCHO	-81.1	5.4	14.1	14.4	13.2	14.4	13.3	13.7	1.9	4.48
DMSO	(CH ₃) ₂ SO	-84.5	4.0	15.4	16.1	14.8	15.5	14.7	14.9	2.1	4.63
Formamide	CH ₃ NO	-92.2	1.1	16.2	17.2	15.1	17.0	15.1	15.9	3.4	4.28
Methylisocyanide	CH ₃ NC	-95.1	-0.5	10.0	10.5	9.5	10.1	8.8	9.0	-1.8	3.59
Nitrobenzene	C ₆ H ₅ NO ₂	-63.6	30.6	34.8	34.8	32.5	—	25.0	25.9	5.4	5.15
Nitromethane	CH ₃ NO ₂	-82.9	5.7	14.2	14.7	13.0	14.7	12.9	13.7	3.5	4.10
Nitrosobenzene	C ₆ H ₅ NO	-125.0	1.0	11.4	—	9.9	—	5.1	6.0	-4.1	3.73
Phenylisocyanide	C ₆ H ₅ NC	-82.7	8.6	16.3	16.5	15.2	16.7	9.0	9.2	-4.9	3.61
Pyridazine	C ₄ H ₄ N ₂	-80.7	20.5	26.3	26.4	25.0	26.7	18.6	19.1	1.7	4.41
Vinylene carbonate	C ₃ H ₂ O ₃	-82.5	20.9	27.2	27.4	26.4	27.7	25.1	25.5	10	5.05
MAE		105.3	8.8	2.8	3.4	2.3	2.4	0.8	Ref.	12.0	

4.1.2 Performance of EA-EOM-CC2 on Valence Bound Radical Anion States of Quinones

Table 4.2: EA-EOM-CC2 benchmark for quinone VBS. Reference values from literature⁴⁹ include experimental (adiabatic) electron affinities and CCSD(T) calculations using aug-cc-pVDZ basis set with LPNO-CCSD extrapolation to higher cardinal numbers. The RI-CC2 calculations employed three basis sets: aug-cc-pVTZ+6s3p (abbreviated as VTZ+) built as described in section 3, standard aug-cc-pVTZ (VTZ), and aug-cc-pVDZ (VDZ).

Molecule	#	Ref. ⁴⁹		RI-CC2			
		Exp.	CCSD(T) +E _{CBS}	SCS VTZ+	No SCS		
					VTZ+	VTZ	VDZ
Benzoq.	1	1.91	1.64	1.54	2.02	2.02	1.81
Methylbenzoq.	2	1.85	1.57	–	1.95	1.95	1.74
2,5-Dimethylbenzoq.	3	1.76	1.49	1.39	1.89	1.89	1.68
2,6-Dimethylbenzoq.	4	1.77	1.50	1.40	1.89	1.89	1.68
Trimethylbenzoq.	5	1.69	1.43	1.34	1.84	1.84	1.63
Duroq.	6	1.62	1.42	1.32	1.83	1.83	1.62
2,6-Dimethoxybenzoq.	7	1.72	1.32	1.17	1.65	1.65	1.43
Ubiqu. (Q ₀)	8	1.86	1.50	1.39	1.88	1.88	1.66
Naphthoq.	9	1.81	1.55	–	1.97	1.97	1.76
2-Methylnaphthoq.	10	1.74	1.51	1.45	1.92	1.91	1.71

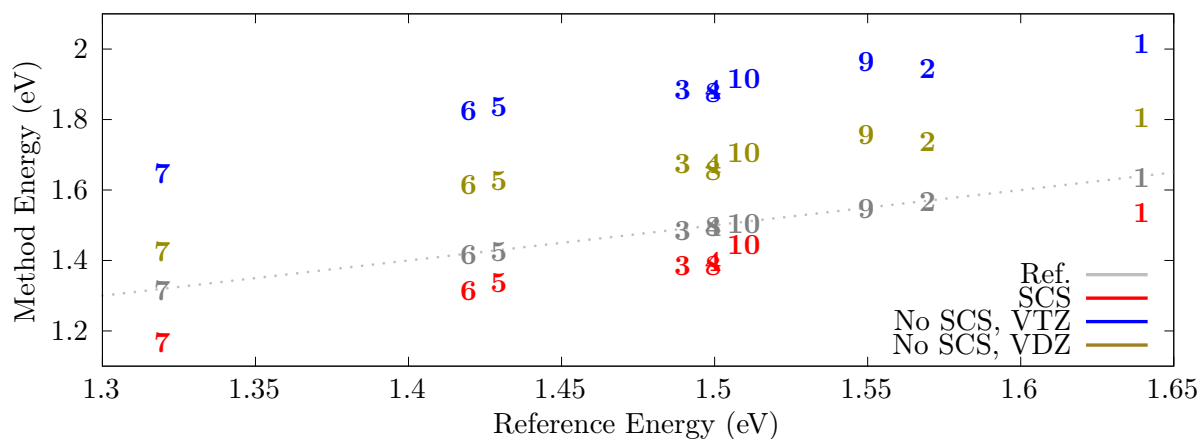


Figure 4.1: Graphical comparison of RI-CC2 methods for quinones. Each point is represented by the compound number given in Table 4.2. The dashed line indicates the reference CCSD(T)+E_{CBS} values.

The performance of EA-EOM-CC2 in calculating the VBS of quinones is benchmarked using a previously established test set of 10 quinones⁴⁹. The results are summarised in Table 4.2 and Figure 4.1. The table includes experimental adiabatic electron affinities and theoretical CCSD(T)+E_{CBS} reference values.

Previous studies have demonstrated that CC2 typically performs poorly for VBSs; however, the implementation of spin-component scaling (SCS) corrections markedly enhances the accuracy of CC2 for these states⁵¹. The RI-CC2 results presented here include calculations both with and without SCS corrections, utilising two different basis sets: VTZ (aug-cc-pVTZ) and VDZ (aug-cc-pVDZ).

The incorporation of SCS improves the accuracy of CC2 for valence-bound states, corroborating the findings of Ref. 51. In general unscaled EA-EOM-RI-CC2 overbinds the electron, and the inclusion of SCS results in a slight underbinding. When comparing the results to experimental data, CC2 might appear to provide better agreement than CCSD. This apparent discrepancy arises because the experimental measurements represent adiabatic electron affinities, whilst the calculations determine vertical electron affinities.

As with the case of DBSs, a smaller cardinality leads to a cancellation of errors in the CC2 binding energies, resulting in apparently more exact results (though arising from more inaccurate calculations). Regarding the inclusion of diffuse functions necessary for modelling DBSs, these have no impact on the VBS energy, indicating that such functions do not contribute to the description of the VBS.

It is noteworthy, however, that in all cases, the CC2 method reproduces the correct trend, as illustrated in Figure 4.1. The error introduced remains remarkably consistent across different molecules. Subsequent calculations omit SCS, as both DBS and VBS states can be obtained from the same Hamiltonian; one can expect a systematic overbinding of ~ 0.2 eV ensuring consistency in the results.

It is also important to note that DBS predictions are known to deteriorate significantly when SCS is applied⁵¹. This is explained by the nature of the DBS; the additional electron is situated far from the core electrons, resulting in a substantially weaker exchange interaction compared to the Coulomb interaction. This characteristic diminishes the effectiveness of SCS for such systems.

4.1.3 Photoelectron Cross-section from EOM-CC2/CCSD

As a part of this work, Dyson orbitals between EOM-CC2 states has been implemented within the `ccman2` module of the *Q-Chem* software package. To evaluate their quality, one must extend beyond mere visual assessment.

Photodetachment cross-sections for 24 valence bound and dipole bound states were calculated using the *ezDyson* package^{106,107}. These calculations employ orbitals from three different sources: EOM-CC2 Dyson orbitals, EOM-CCSD Dyson orbitals and the dominant Hartree-Fock orbital. The complete results can be found in appendix B. Figure 4.2 shows two representative examples: the valence bound state of azulene and the dipole bound state of nitromethane.

The results demonstrate that EOM-CC2 successfully captures the essential features of the cross-section, appearing nearly identical in the case of nitromethane’s dipole-bound state and showing only minor deviations for azulene. In contrast, using HF orbitals as approximations for Dyson orbitals fails to reproduce the shape obtained with EOM-CCSD. Although a single HF orbital typically dominates the Dyson orbital composition¹⁰⁸, the contributions from additional electronic configurations introduced by the correlation prove to be significant.

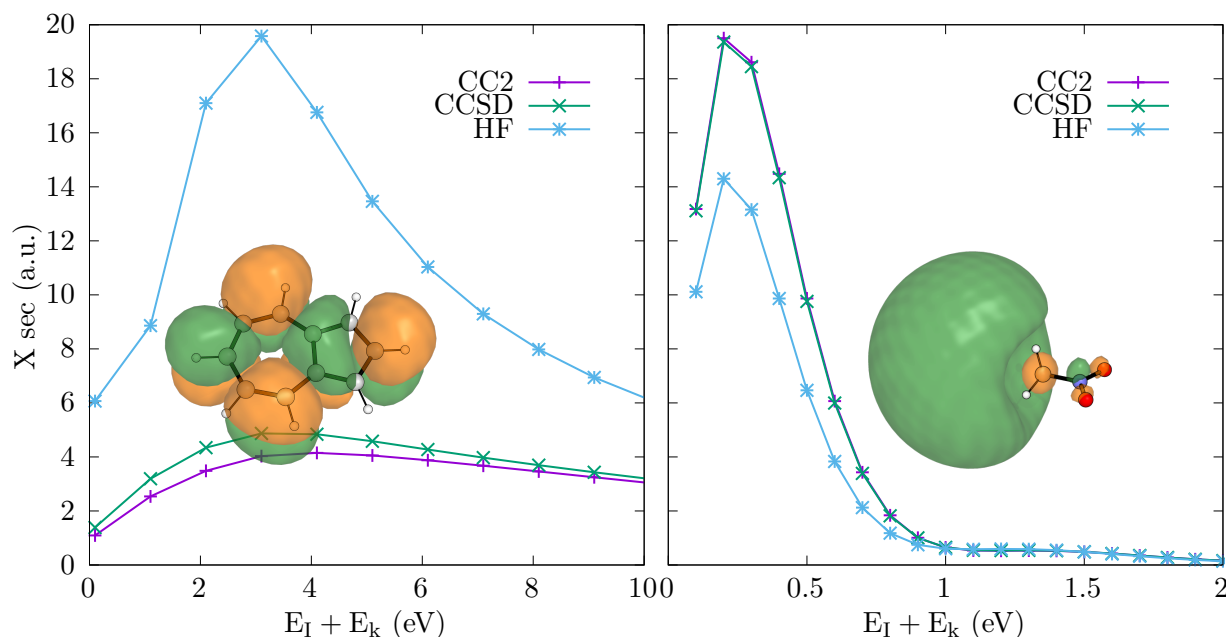


Figure 4.2: Photoelectron detachment cross-sections of azulene (VBS) and nitromethane (DBS). The cross-sections were calculated using Dyson orbitals from EOM-CC2, EOM-CCSD and the highest populated HF orbital. The corresponding EA-EOM-CC2 Dyson orbitals are also shown as insets.

4.2 Study on the Anion States of Ubiquinone

Having benchmarked the performance of the methods has been assessed, the focus shifts to the anion states of ubiquinone (CoQ). The results presented here are based on the calculations performed with RI-EA-EOM-CC/aug-cc-pVDZ+6s3p.

4.2.1 Energy and Dipole Surfaces of CoQ

Surfaces of Q0

The conformational landscape of the simplest ubiquinone, Q_0 , was investigated by varying the dihedral angles of the methoxy chains relative to the quinone plane in steps of 20° , as shown in Figure 4.4. These dihedral angles represent the most significant degrees of freedom in the system, as the remainder of the molecule is relatively rigid. This approach

enables the construction of potential energy surfaces (PES), dipole strength surfaces, and anionic (VBS and DBS) surfaces, as depicted in Figure 4.3. Owing to the C_2 symmetry present when the methoxy chains are coplanar, only half of the surface points require sampling.

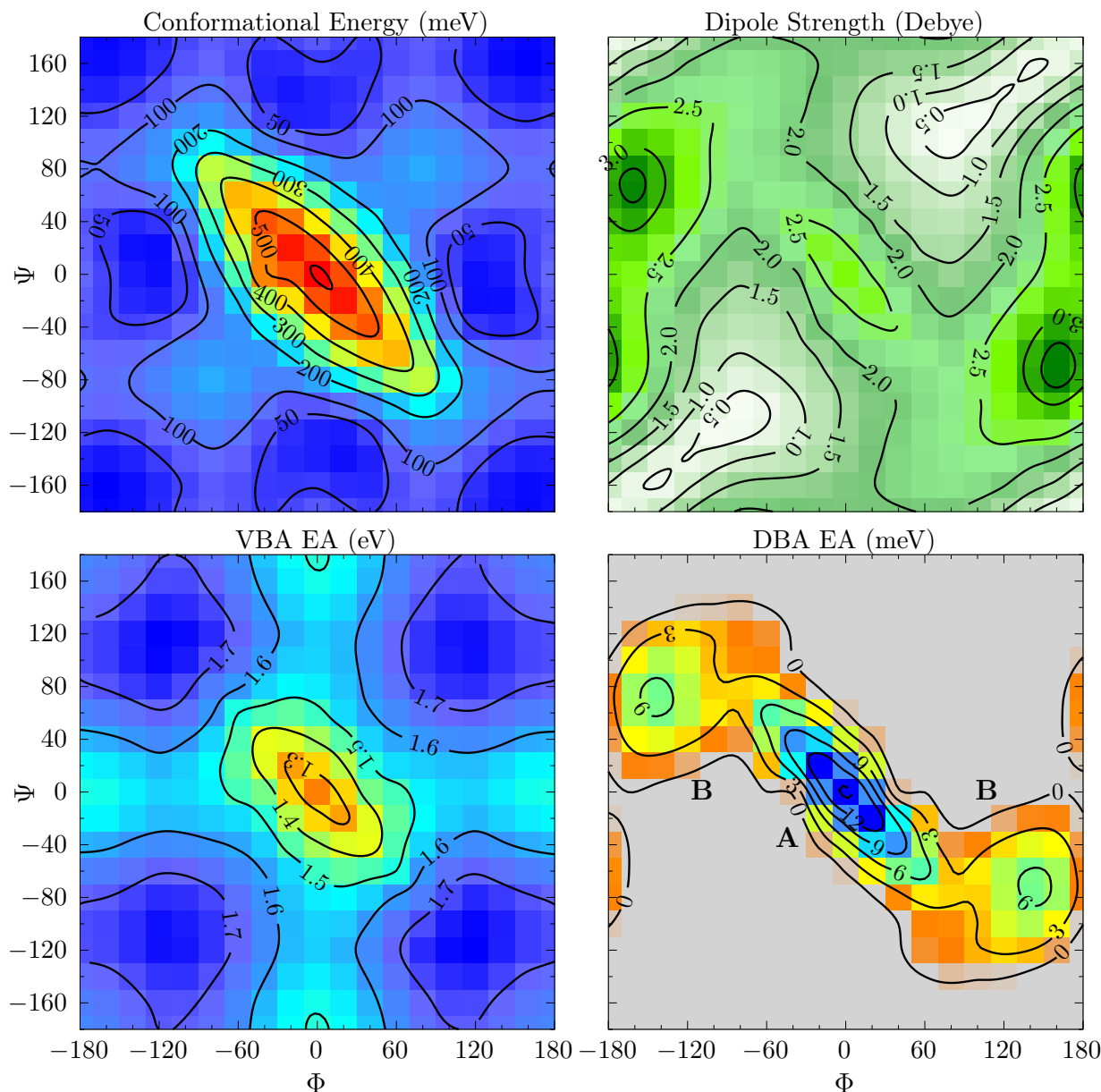


Figure 4.3: Surfaces of Q0. From left to right and top to bottom: potential energy surface (CC2), dipole moment surface (DFT TPSS), vertical binding energy surface (EA-EOM-CC2), and dipole bound anion surface (EA-EOM-CC2) of Q0. Gray points the DBS surface indicate predicted unbound states.

The conformational energy surface of the neutral molecule reveals five minima, corresponding to configurations where the methoxy groups are oriented away from each other. The global minimum occurs at $(180,180)$, where both chains are coplanar with the quinone and directed oppositely. Four additional minima are found at $(\pm 140, \mp 20)$ and

($\pm 20, \mp 140$), each approximately 10 meV above the global minimum. The presence of a methyl group at position 5 slightly perturbs the symmetry between the methoxy chains, but its influence on the energy landscape is minimal due to its spatial separation. The energy barriers separating these wells range from 65 to 100 meV, suggesting that inter-conversion between conformers is feasible at ambient temperature. A pronounced steric repulsion is observed near (0,0), where both methoxy chains are coplanar and oriented towards each other, resulting in an energy penalty of approximately 580 meV.

The dipole strength surface largely reflects the vector sum of the individual methoxy group dipoles. When both chains are aligned in the same direction, the dipole strength is maximised, and vice versa. The lowest dipole moment, below 0.5 Debye, is found near (180,180). Local maxima in dipole strength are observed at (0,0) with a strength of 2.5 D, and ($\pm 160, \mp 80$) ($\mu = 3.2$ D), ($\pm 60, \mp 160$) ($\mu = 3.4$ D), and ($\pm 80, \pm 180$) ($\mu = 3.2$ D), with the latter two coinciding with conformational minima at ($\pm 140, \mp 20$).

The valence-bound state (VBS) surface can be rationalised by considering the electron-withdrawing effect of out-of-plane methoxy groups and the electron-donating effect of in-plane conjugation. The VBS minimum is observed at four points where both chains are approximately $\pm 120^\circ$ out of plane, with a vertical electron affinity (VAE) of 1.77 eV. Notably, when either chain is coplanar ($\pm 0^\circ$), the VAE increases by about 0.2 eV. The global minimum occurs at (0,0), where both chains are in-plane, with a VAE of 1.26 eV. The pronounced dependence of the electron affinity on methoxy conformation has been proposed as a mechanism to control the electron transfer processes in quinone redox enzymes^{49,80,109–111}.

The dipole-bound state (DBS) surface, as anticipated, closely follows the dipole strength surface. It is important to note that in regions where the DBS is unbound, the EA-EOM-CC2 values are not physically meaningful and would approach the continuum in the basis set limit. Three distinct regions are apparent, mirroring those of the dipole strength surface. The region at ($\pm 60, \pm 180$) ($\mu = 3.1$ D) is the smallest and most weakly bound, with only five points exhibiting binding energies up to 2 meV. Region B in Figure 4.3, centred at ($\pm 140, \mp 20$) ($\mu = 3.2$ D), is more extensive and reaches a maximum binding energy of 6.2 meV. Region A, at (0,0), is the most strongly bound, with a maximum of 15.8 meV, despite its lower dipole strength. This may be attributed to the orientation of the dipole moment: in region B, the dipole points above the quinone, and the DBS electron density interacts repulsively with the π system, whereas in region A, the dipole is directed away from the quinone plane. In Figure 4.4, these cases are shown.

Surprisingly, CC2 predicts DBSs in region A supported by dipole moments as small as 1.6D, which is significantly lower than the commonly cited threshold of 2.5D and falls within the range of the ideal dipole DBS⁸. This result suggests that, in addition to the excess electron density being spatially separated from the valence electrons, further

stabilisation arises from dispersion interactions with the π system. Effects similar to this have been experimentally observed in indolide anions¹¹². Nevertheless, the high conformational energy of region A makes its population unlikely.

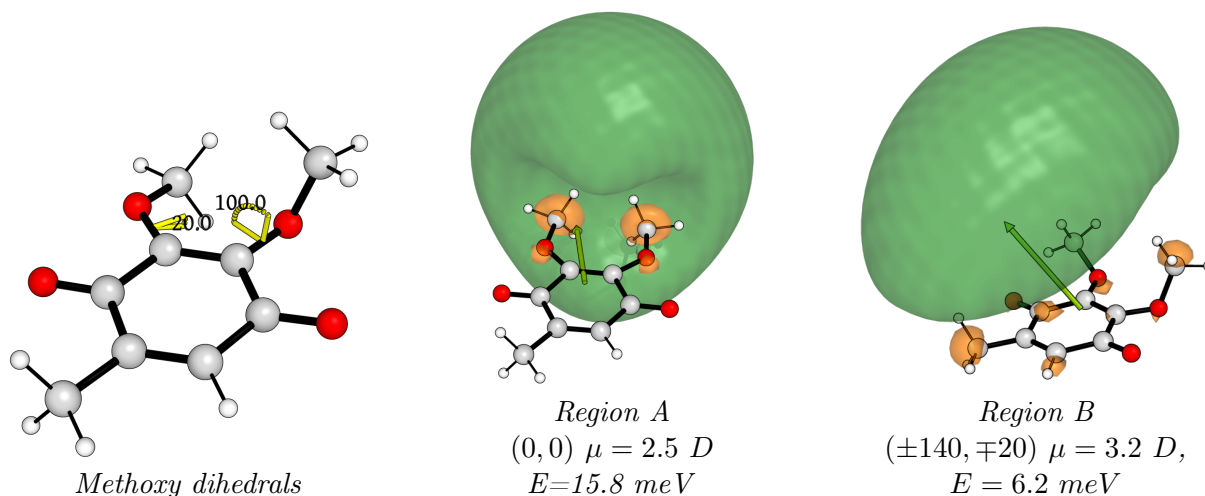


Figure 4.4: Dyson orbitals of Q0 calculated with RI-EA-EOM-CC/aug-cc-pVDZ+6s3p. The left panel explicitly shows the methoxy dihedral coordinates. The middle panel shows the Dyson orbital of the strongest bound DBS from region B. The right panel shows the Dyson orbital strongest bound DBS from region A. The isosurface is set to 0.005 e/Bohr³ and the dipole moment vector is shown as a green arrow with origin at the centre of mass.

Surfaces of Q1

The isoprene tail introduces additional degrees of freedom, resulting in a more complex conformational landscape. To investigate its effect, the analogous surfaces for Q₁ were constructed by fixing the bend and dihedral angles of the isoprene unit relative to the quinone plane to the crystal structure of the quinone in the active site of bacterial complex I (PDB: 6I0D)⁷⁴, as presented in Figure 4.6. The results are shown in Figure 4.5. In this case, we remove the plane of symmetry of the molecule, and all points of the surface have to be sampled. The PES and dipole surfaces were calculated using TPSS functional (DFT). Due to the computational cost, only the points with a dipole strength above 1.6 Debye were sampled.

Concerning the conformational potential energy surface (PES), the fixed position of the isoprene tail, distant from the quinone moiety, prevents interaction with the methoxy chains. This renders the scenario largely analogous to that of Q₀. Steric hindrances would be anticipated with longer tails or alternative configurations. However, the realism of this particular system is questionable, as crystallographic data¹¹⁰ indicate that the isoprene tail does not penetrate the quinone moiety's pocket. Within a protein, the orientation of the methoxy chains is dictated by the local environment, with specific configurations favoured by interactions with first-shell amino acids.

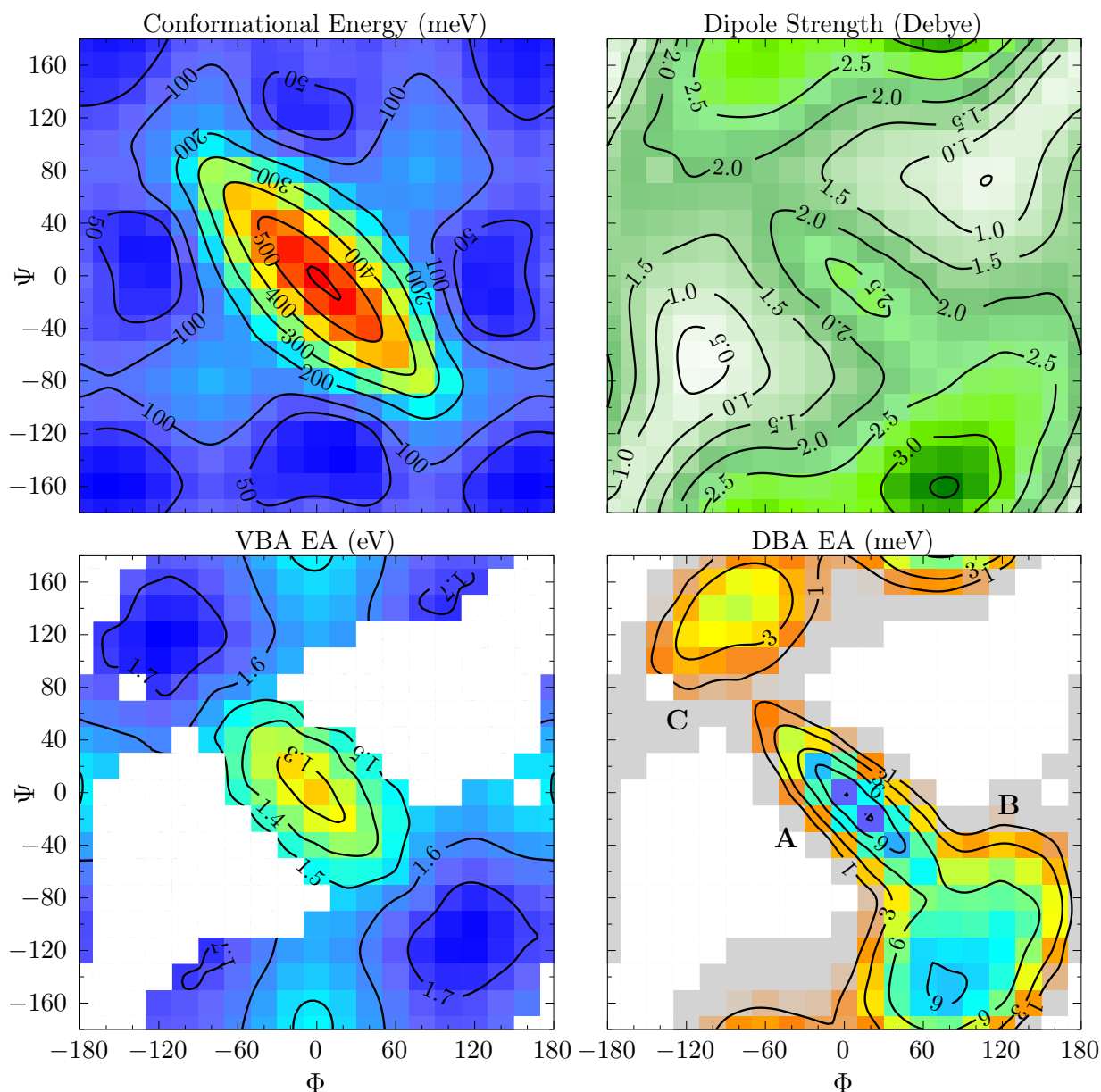


Figure 4.5: From left to right and top to bottom: Energy surface (DFT TPSS), dipole moment surface (DFT TPSS), vertical binding energy surface (EA-EOM-CC2), and dipole bound anion (EA-EOM-CC2) surface of Q1. White points in VBS and DBS surfaces were not sampled, gray points indicate predicted unbound states.

The interpretation of the dipole strength surface is also similar to that of Q₀, with the addition of a fixed dipole originating from the isoprene group, which is oriented approximately out of the plane. This has the effect of dividing region B from Figure 4.3 into two distinct regions for Q₁, designated B and C. In region B, the local dipole of the isoprene aligns with the methoxy dipoles, resulting in a maximum dipole strength of 3.3 Debye at (160,-80). Conversely, in region C, destructive interference occurs between the local dipoles, leading to a maximum dipole strength of 2.9 Debye at (-60,160). Region A is only slightly affected, retaining a maximum dipole strength of 2.6 D at (0,0).

The VBS surface of Q_1 is more challenging to interpret due to the omitted data points. Nevertheless, the overall picture appears to remain consistent, as the qualitative effect of the rotation of the chains (acting as electron donor or acceptor) is unchanged. The range of vertical electron affinity (VEA) varies surprisingly little, with a global minimum of 1.26 eV at (0,0) and a maximum of 1.76 eV at (-120,120). It had been previously proposed that, contrary to its established spectator role, the isoprene tail might contribute to the stabilisation of the excess electron⁴². However, the results presented herein suggest that the isoprene tail does not significantly affect the VBS of Q_1 , at least in the conformation employed in this study.

Regarding the DBS surface, the impact of the isoprene tail is more pronounced. In region B, where the local dipole of the isoprene tail aligns with the methoxy dipoles, the region expands to encompass a larger area and exhibits a maximum binding energy of 9.1 meV at (80,-160). In region C, the local dipoles interfere destructively, resulting in a smaller area with a maximum binding energy of 5.0 meV at (-80,140). Region A shows a minor difference, with a maximum binding energy of 12.2 meV at (20,-20). In Figure 4.6, the Dyson orbitals of the structures are shown. The variations in electron binding energy in regions B and C can be attributed to changes in the dipole moment strength. The alteration in region A, however, is likely related to a decrease in the favourable interactions between the DBS and the rest of the electronic density, as the dipole moment remains largely unchanged. Finally, it is again noteworthy the prediction of structures with dipole moments below 2.5 D, which are predicted to be bound by EA-EOM-CC2; with dihedrals of (20,20) and dipole of 1.81 D, the binding energy is 2.2 meV.

An important consideration for dipole-bound states (DBS) is the extent of correlation between their binding energy and the strength of the dipole moment that supports them. The DBS maps for Q_0 , Figure 4.3, and Q_1 , Figure 4.5, are clearly demarcated into distinct regions. Figure 4.7 presents a scatter plot illustrating all bound points for both Q_0 and Q_1 . This plot demonstrates that the different regions identified in the maps correspond to separate populations in the scatter data. A correlation between dipole strength and binding energy is observed in all regions, though the degree of this correlation varies. For instance, region A, which accommodates the strongest dipoles, exhibits a nearly linear relationship between these two parameters for both quinones. This behaviour can be attributed to its conceptual similarity to an ideal dipole. When comparing region A in Q_0 and Q_1 , the slope for Q_0 is steeper than that for Q_1 , indicating that variations in the chemical environment affect the interplay between the dipole moment and the binding strength.

Concerning the populations in regions B and C, the relationship between the dipole moment and binding energy is considerably less pronounced. This is likely because the DBS occupies a spatial region closer to the other electrons, specifically the π system. In

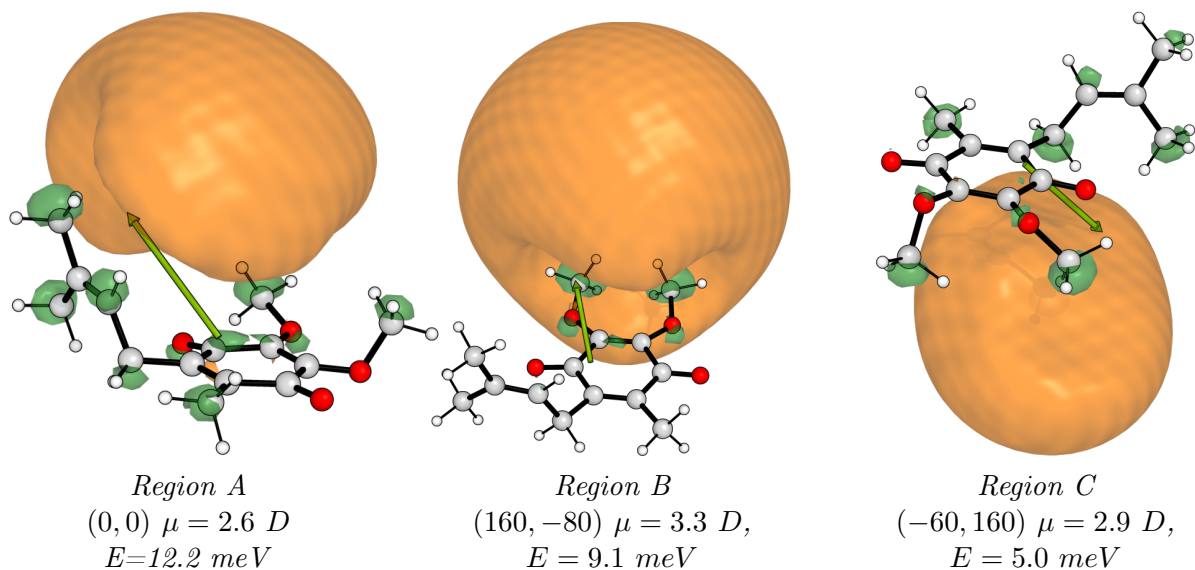


Figure 4.6: Dyson orbitals of Q0 calculated with RI-EA-EOM-CC/aug-cc-pVDZ+6s3p. The left panel shows the Dyson orbital of the strongest bound DBS from region A. The middle panel shows the Dyson orbital of the strongest bound DBS from region B. The right panel shows the Dyson orbital strongest bound DBS from region A. The isosurface is set to 0.005 e/Bohr^3 and the dipole moment vector is shown as a green arrow with origin at the centre of mass.

this system, alterations in dipole strength arise from changes in its orientation. Consequently, the displacement of the DBS that accompanies the strengthening of the dipole might result in a less favourable interaction with the remaining electronic density. In general, the electron binding energy is only loosely correlated with the magnitude of the dipole moment that supports it. However, for analogous systems, such as region A, these two quantities become more significantly interconnected.

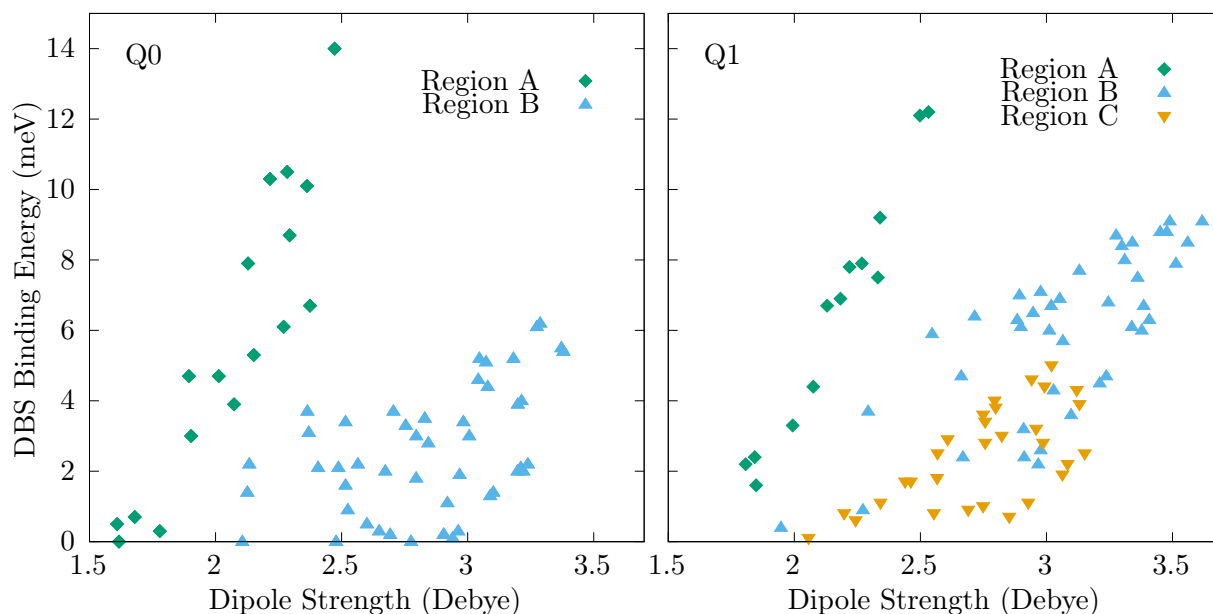


Figure 4.7: Q_0 and Q_1 DBS populations assigned to the DBS surfaces from Figures 4.3 and 4.5.

4.2.2 Interaction with small molecules

Subsequent to the characterisation of the isolated quinones, the focus shifts to the interaction of their anionic states with small molecules. Recognising that chemical processes in nature do not occur in a vacuum and that environmental interactions are crucial, this work investigates these effects by considering small molecular clusters. Figure 4.8 detail the interactions between Q_0 , region B, with a dipole of 3.4 Debye, and selected molecules: methane, ammonia (1.47 D), water (1.85 D), and hydrogen fluoride (1.82 D). For these model systems, the dipole of the solvent molecule was oriented to interact either constructively or destructively with the quinone's dipole. In the case of methane, which has no dipole moment, it is shown in both cases for comparison. The intermolecular distance was systematically varied from 30 down to 4 Å. The consequent effects on the VBS and DBS energies, are presented. It is important to note that none of these molecules support an anionic state on their own. The DBS of a representative $Q_0 + \text{water}$ system for each of the two orientations is shown in Figure 4.6.

Considering the DBS, when the solvent and quinone dipoles are opposed, polar molecules induce a wide well with a minimum at around 8 Å. The electron binding energy of the DBS reaches 60 meV with both water and HF, and 37 meV with ammonia. This represents a more than tenfold increase compared to the 5.4 meV binding energy of the isolated quinone. Stabilisation by methane is considerably weaker, as it arises solely from dispersion forces. The similarity between the water and HF interaction curves is noteworthy; they overlap almost perfectly across most of the separation range. This congruence is attributed to their comparable dipole moments (1.85 D for water; 1.82 D for HF). At large separations, the specific electronic structures of these solvent molecules are less influential, and the DBS primarily experiences the effect of their dipole moments. The interaction with ammonia is weaker due to its smaller dipole moment of 1.47 D. This scenario is characteristic of a solvated electron within a 'cavity'^{8,57}. At an intermolecular distance of approximately 4 Å, the interaction becomes repulsive for all molecules studied due to steric interactions, causing the DBS to become unbound due to steric hindrance.

Conversely, with parallel dipole orientations, polar molecules exhibit repulsion at large distances. This is attributable to the negative end of the solvent dipole destabilising the DBS. At shorter ranges, however, the local dipoles combine constructively, thereby stabilising the binding energy. For water, which possesses the largest dipole moment, the DBS attains an electron binding energy of 80 meV, with the total system dipole moment being 6.1 Debye. Such configurations have recently been observed in photoelectron spectroscopy experiments²¹ and are thought to play an important role in the transfer of a VBS to a solvated electron.

The interaction also significantly affects the VBS. When the dipoles are opposed, *i.e.*,

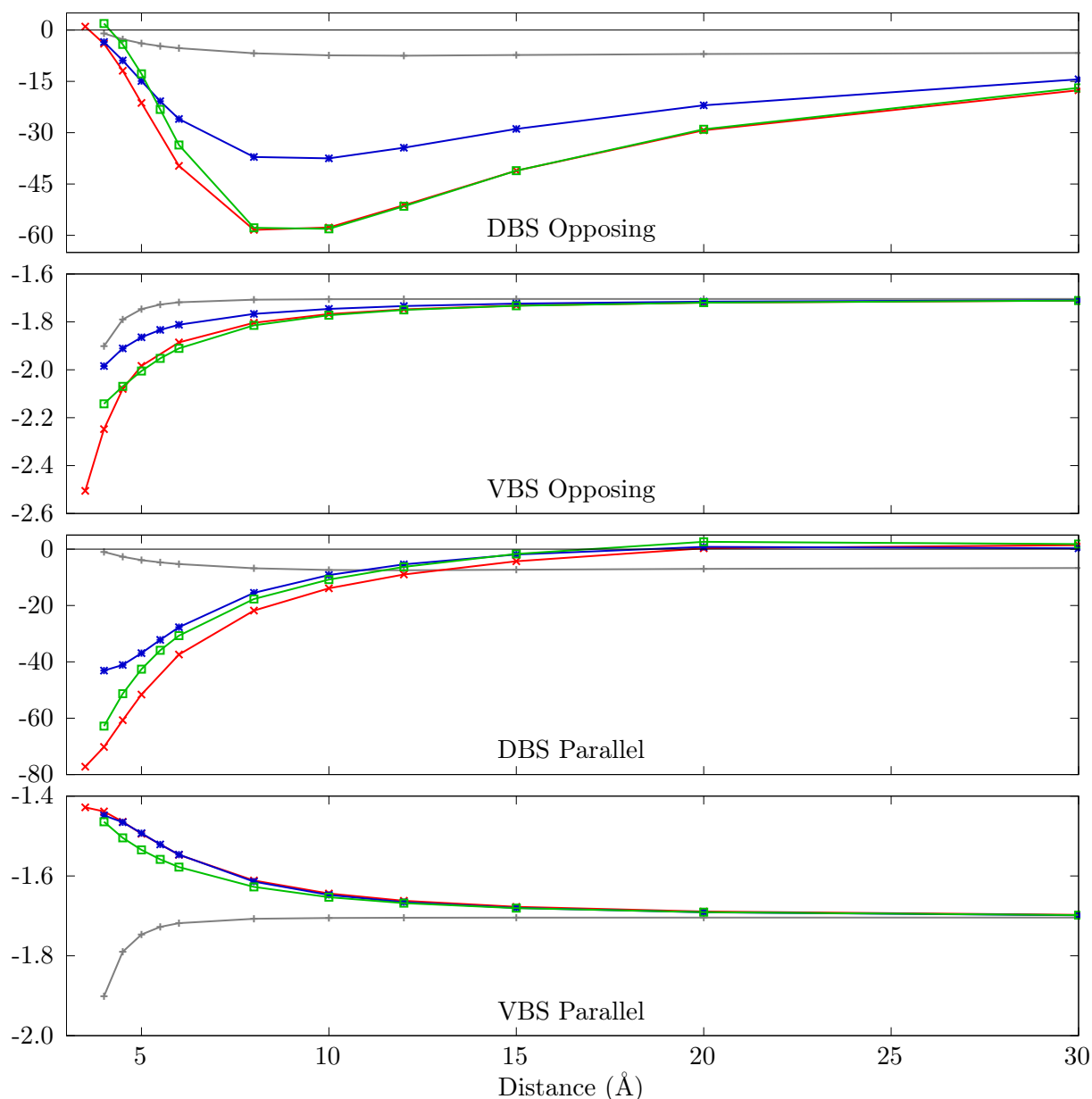


Figure 4.8: Q_0 interaction with small molecules. From top to bottom: DBS with opposing dipoles, VBS with opposing dipoles, DBS with aligned dipoles, and VBS with aligned dipoles.

the positive end of the solvent dipole is oriented towards the excess electronic charge of the quinone, the VBS is strongly stabilised at short intermolecular distances. With water, the VBS achieves a VEA of 2.5 eV, an increase of over 0.8 eV compared to the isolated quinone. A similar effect is observed for HF, yielding a VEA of 2.5 eV, while the stabilisation is less pronounced for ammonia and methane. A comparison of the influence of surrounding molecules on the VBS with that of methoxy chain rotation, as discussed in section 4.2.1, reveals that intermolecular interactions can be considerably more influential. The protein environment has probably a larger effect on the CoQ EA than the orientation adopted by the methoxy chains.

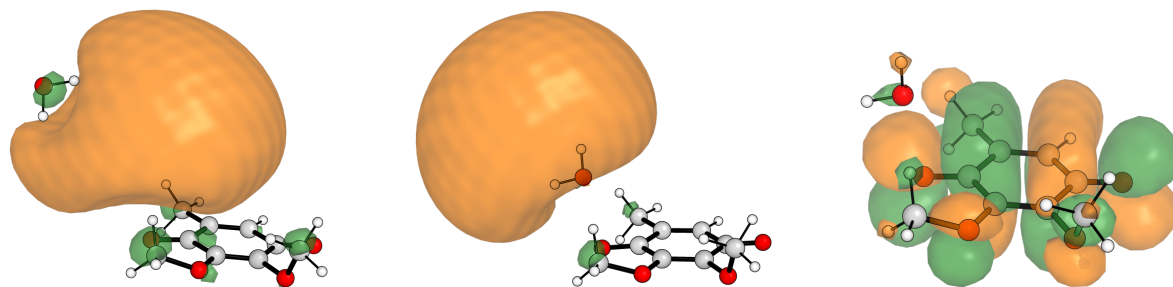


Figure 4.9: Dyson orbitals of Q0 + water. Left, system where the dipoles are pointing in opposed directions at an intermolecular distance of 8 Å. Middle: dipoles aligned at an intermolecular distance of 4 Å. Right: VBS of Q0 and a water molecule at 4 Å. The isosurface is set to 0.01 e/Bohr³.

If the dipoles are aligned, the negative end of the solvent dipole interacts with the VBS and is destabilised. A similar and unfavourable trend is observed for the three polar molecules. At an intermolecular distance of 4 Å, the VEA decreases to approximately 1.4 eV. The destabilisation arises from the negative end of the solvent dipole repelling the excess electron density of the quinone.

Chapter 5

Conclusion and Outlook

This thesis presents a theoretical investigation of anionic states of ubiquinone, which supports both a dipole-bound state and valence-bound states, primarily through equation-of-motion coupled-cluster (EOM-CC) techniques. The principal objectives included benchmarking EOM-CC2-based approaches, assessing basis set considerations for DBSs, implementing Dyson orbitals for EOM-CC2, and applying these methods to ubiquinone (CoQ) analogues, Q_0 and Q_1 .

Scrutiny of basis set dependence for EA-EOM-CC2 revealed that, although larger cardinality sets (e.g. aug-cc-pVTZ) are often beneficial, the inclusion sufficiently diffuse functions is critical for describing the spatial extension of DBS orbitals. In general CC2 tends to overbind these states when compared to CCSD.

For VBSs, EA-EOM-CC2 was benchmarked against known quinones, showing that spin-component scaling (SCS) notably improves accuracy relative to uncorrected CC2. EA-EOM-CC2-SCS tends to slightly underbind the VBS states. However, unscaled CC2 has a consistent error and is able to recover the trends. The diffuse functions integral to DBSs had minimal impact on VBS energies, as they are much more localized in space.

A methodological advance was the implementation of EOM-CC2 Dyson orbitals. Their quality was assessed by comparing them to EOM-CCSD Dyson orbitals and HF orbitals in the calculation of photodetachment cross-sections. Validating EOM-CC2 Dyson orbitals as a resource-efficient alternative to EOM-CCSD.

Investigations of Q_0 revealed the interplay between methoxy chain conformations and the resulting potential energy, dipole moment, VBS, and DBS surfaces. Five minima were detected on the neutral PES, with methoxy group orientations dictating the dipole moment and hence affecting DBS energies.

Extending to Q_1 , the attached isoprene tail altered the overall molecular dipole to create changes in DBS binding, with constructive dipolar alignment enhancing DBS stability and destructive alignment reducing it. The VBS of Q_1 was not particularly sensitive to the isoprene tail's presence. Different modes of DBS stabilization were observed, depending

on their interaction with the rest of that electronic density. Within each mode, or region, the DBS binding strength seems to be correlated strongly with dipole magnitude.

Preliminary explorations of interactions between Q_0 and small molecules (methane, ammonia, water, HF) underscored the sensitivity of both VBSs and DBSs to the local environment. This outcome emphasises the importance of considering environmental effects, which is essential to model states in condensed-phase or biological settings.

Overall, this thesis advances the understanding of non-valence anionic states and the computational techniques applied to them. The benchmarking of EA-EOM-CC2 furnishes guidelines for those seeking cost-effective yet reliable estimates of electron affinities, DBSs, and VBSs, while confirming the utility of EOM-CC2 Dyson orbitals in photodetachment studies. The exploration of ubiquinone anion states underscores how molecular conformation and local electrostatic factors govern the stability and character of both VBSs and DBSs. The observation of DBSs supported by smaller dipole moments challenges common assumptions, highlighting the relevance of dispersion-type interactions in NVs.

From a pedagogical perspective, this work comprehensively spans multiple facets of theoretical chemistry and computational modelling. Starting from the bottom with a derivation of an algebraic expression for EOM-CC2 Dyson orbitals, progresses to their implementation in commercial quantum-chemistry software, and culminates in their application to a sizeable (*bio*)chemical challenge: the anionic states of ubiquinone.

Despite these contributions, several directions for further work remain:

- **Advanced Solvation Models:** Though small-molecule interactions were considered, explicit solvation or hybrid QM/MM simulations could quantitatively characterise environmental influence on VBS and DBS formation in solution or protein settings. Other techniques that could be utilised is electrostatic embedding.
- **Dynamic Effects:** For larger systems that include more solvating molecules, introducing molecular dynamics simulations to account for structural fluctuations would offer insights into anion state energies and interconversions under realistic conditions.
- **Relating to Experimental Observables:** Future efforts could concentrate on predicting and interpreting experimental data, such as electron transmission, photoelectron angular distributions, or connecting VBS/DBS energies to redox properties in electrochemical or biochemical contexts. Specifically, one could compute the nonadiabatic couplings between a potential electron donor state and the VBS and

In summary, this thesis offers a thorough computational analysis of non-valence anions, supplies methodological insights, and delivers a closer characterisation of ubiquinone anion

states. These outcomes pave the way for further studies of the complex physics and chemistry associated with such species in larger or more intricate biological frameworks.

Bibliography

- (1) Simons, J. *The Journal of Physical Chemistry A* **2008**, *112*, 6401–6511.
- (2) Simons, J. *The Journal of Physical Chemistry A* **2023**, *127*, 3940–3957.
- (3) Simons, J. *Annual Review of Physical Chemistry* **2011**, *62*, 107–128.
- (4) Herbert, J. M. *Reviews in Computational Chemistry Volume 28* **2015**, 391–517.
- (5) Fermi, E.; Teller, E. *Physical Review* **1947**, *72*, 399.
- (6) Desfrancois, H. *Int. J. Mod. Phys. B* **1996**, *10*, 1339.
- (7) Gutowski, M.; Skurski, P.; Boldyrev, A. I.; Simons, J.; Jordan, K. D. *Physical Review A* **1996**, *54*, 1906.
- (8) Jordan, K. D.; Wang, F. *Annual review of physical chemistry* **2003**, *54*, 367–396.
- (9) Qian, C.-H.; Zhu, G.-Z.; Wang, L.-S. *The journal of physical chemistry letters* **2019**, *10*, 6472–6477.
- (10) Jordan, K. D.; Liebman, J. F. *Chemical Physics Letters* **1979**, *62*, 143–147.
- (11) Desfrancois, C.; Bouteiller, Y.; Schermann, J.; Radisic, D.; Stokes, S.; Bowen, K.; Hammer, N.; Compton, R. *Physical review letters* **2004**, *92*, 083003.
- (12) Sommerfeld, T.; Dreux, K. M.; Joshi, R. *The Journal of Physical Chemistry A* **2014**, *118*, 7320–7329.
- (13) Sommerfeld, T.; Bhattarai, B.; Vysotskiy, V. P.; Cederbaum, L. S. *The Journal of chemical physics* **2010**, *133*.
- (14) Voora, V. K.; Cederbaum, L. S.; Jordan, K. D. *The journal of physical chemistry letters* **2013**, *4*, 849–853.
- (15) Voora, V. K.; Jordan, K. D. *The Journal of Physical Chemistry A* **2014**, *118*, 7201–7205.
- (16) Voora, V. K.; Kairalapova, A.; Sommerfeld, T.; Jordan, K. D. *The Journal of Chemical Physics* **2017**, *147*.
- (17) Schiedt, J.; Weinkauf, R.; Neumark, D. M.; Schlag, E. *Chemical Physics* **1998**, *239*, 511–524.

- (18) Jalbout, A.; Adamowicz, L. *The Journal of Physical Chemistry A* **2001**, *105*, 1033–1038.
- (19) Gutowski, M.; Hall, C.; Adamowicz, L.; Hendricks, J.; De Clercq, H.; Lyapustina, S.; Nilles, J.; Xu, S.-J.; Bowen Jr, K. *Physical review letters* **2002**, *88*, 143001.
- (20) Eustis, S.; Wang, D.; Lyapustina, S.; Bowen, K. H. *The Journal of chemical physics* **2007**, *127*.
- (21) Clarke, C. J.; Michi Burrow, E.; Verlet, J. R. *Nature Communications* **2025**, *16*, 2113.
- (22) Hendricks, J.; Lyapustina, S.; De Clercq, H.; Bowen, K. *The Journal of chemical physics* **1998**, *108*, 8–11.
- (23) Sommerfeld, T. *Physical Chemistry Chemical Physics* **2002**, *4*, 2511–2516.
- (24) Sommerfeld, T. *The Journal of Physical Chemistry A* **2004**, *108*, 9150–9154.
- (25) Sommerfeld, T. In *Journal of Physics: Conference Series*, 2005; Vol. 4, p 245.
- (26) Verlet, J. R.; Anstoter, C. S.; Bull, J. N.; Rogers, J. P. *The Journal of Physical Chemistry A* **2020**, *124*, 3507–3519.
- (27) Kang, D. H.; Kim, J.; Eun, H. J.; Kim, S. K. *Accounts of Chemical Research* **2022**, *55*, 3032–3042.
- (28) Hassan, S. Z.; Tauch, J.; Kas, M.; Nötzold, M.; Carrera, H. L.; Endres, E. S.; Wester, R.; Weidemüller, M. *Nature communications* **2022**, *13*, 818.
- (29) Fortenberry, R. C. *The Journal of Physical Chemistry A* **2015**, *119*, 9941–9953.
- (30) Gu, J.; Leszczynski, J.; Schaefer III, H. F. *Chemical reviews* **2012**, *112*, 5603–5640.
- (31) Narayanan SJ, J.; Tripathi, D.; Verma, P.; Adhikary, A.; Dutta, A. K. *ACS omega* **2023**, *8*, 10669–10689.
- (32) Sedmidubská, B.; Kočišek, J. *Physical Chemistry Chemical Physics* **2024**, *26*, 9112–9136.
- (33) Desfrancois, C. *Physical Review A* **1995**, *51*, 3667.
- (34) Liu, G.; Ciborowski, S. M.; Graham, J. D.; Buytendyk, A. M.; Bowen, K. H. *The Journal of Chemical Physics* **2020**, *153*.
- (35) Rogers, J. P.; Anstoöter, C. S.; Bull, J. N.; Curchod, B. F.; Verlet, J. R. *The Journal of Physical Chemistry A* **2019**, *123*, 1602–1612.
- (36) Clarke, C. J.; Verlet, J. R. *Annual Review of Physical Chemistry* **2024**, *75*.
- (37) Cyr, D. R.; Hayden, C. C. *The Journal of chemical physics* **1996**, *104*, 771–774.
- (38) Neumark, D. M. *Annual review of physical chemistry* **2001**, *52*, 255–277.

- (39) Carles, S.; Desfrancois, C.; Schermann, J.; Berges, J.; Houée-Levin, C. *International Journal of Mass Spectrometry* **2001**, *205*, 227–232.
- (40) Bradforth, S. E.; Jungwirth, P. *The Journal of Physical Chemistry A* **2002**, *106*, 1286–1298.
- (41) Ameixa, J.; Arthur-Baidoo, E.; Pereira-da-Silva, J.; Ončák, M.; Ruivo, J.; Varella, M. d. N.; Da Silva, F. F.; Denifl, S. *Computational and Structural Biotechnology Journal* **2023**, *21*, 346–353.
- (42) Pshenichnyuk, S. A.; Modelli, A.; Asfandiarov, N. L.; Komolov, A. S. *The Journal of chemical physics* **2020**, *153*.
- (43) Skurski, P.; Gutowski, M.; Simons, J. *International Journal of Quantum Chemistry* **2000**, *80*, 1024–1038.
- (44) Thiam, G.; Rabilloud, F. *Journal of Chemical Theory and Computation* **2023**, *19*, 2842–2849.
- (45) Vila, F. D.; Jordan, K. D. *The Journal of Physical Chemistry A* **2002**, *106*, 1391–1397.
- (46) Ivanov, A. S.; Zhang, X.; Wang, H.; Boldyrev, A. I.; Ganteför, G.; Bowen, K. H.; Cernusak, I. *The Journal of Physical Chemistry A* **2015**, *119*, 11293–11303.
- (47) Moorby, R. E.; Parravicini, V.; Alessio, M.; Jagau, T.-C. *Physical Chemistry Chemical Physics* **2024**, *26*, 6532–6539.
- (48) Haldar, S.; Dutta, A. K. *The Journal of Physical Chemistry A* **2020**, *124*, 3947–3962.
- (49) Schulz, C. E.; Dutta, A. K.; Izsák, R.; Pantazis, D. A. *Journal of Computational Chemistry* **2018**, *39*, 2439–2451.
- (50) Christiansen, O.; Koch, H.; Jørgensen, P. *Chemical Physics Letters* **1995**, *243*, 409–418.
- (51) Paran, G. P.; Utku, C.; Jagau, T.-C. *Physical Chemistry Chemical Physics* **2024**, *26*, 1809–1818.
- (52) Coe, J.; Lee, G.; Eaton, J.; Arnold, S.; Sarkas, H.; Bowen, K.; Ludewigt, C.; Haberland, H.; Worsnop, D. *The Journal of chemical physics* **1990**, *92*, 3980–3982.
- (53) Verlet, J.; Bragg, A.; Kammrath, A.; Cheshnovsky, O.; Neumark, D. *Science* **2005**, *307*, 93–96.
- (54) Coe, J. V.; Williams, S. M.; Bowen, K. H. *International Reviews in Physical Chemistry* **2008**, *27*, 27–51.

- (55) Siefermann, K. R.; Liu, Y.; Lugovoy, E.; Link, O.; Faubel, M.; Buck, U.; Winter, B.; Abel, B. *Nature chemistry* **2010**, *2*, 274–279.
- (56) Kumar, A.; Walker, J. A.; Bartels, D. M.; Sevilla, M. D. *The Journal of Physical Chemistry A* **2015**, *119*, 9148–9159.
- (57) Herbert, J. M. *Physical Chemistry Chemical Physics* **2019**, *21*, 20538–20565.
- (58) Herbert, J. M.; Coons, M. P. *Annual review of physical chemistry* **2017**, *68*, 447–472.
- (59) Kevan, L. *Accounts of Chemical Research* **1981**, *14*, 138–145.
- (60) Anusiewicz, I.; Skurski, P.; Simons, J. *The Journal of Physical Chemistry A* **2020**, *124*, 2064–2076.
- (61) Castellani, M. E.; Anstöter, C. S.; Verlet, J. R. *Physical Chemistry Chemical Physics* **2019**, *21*, 24286–24290.
- (62) Larsen, R. E.; Glover, W. J.; Schwartz, B. J. *Science* **2010**, *329*, 65–69.
- (63) Narayanan SJ, J.; Verma, P.; Adhikary, A.; Kumar Dutta, A. *ChemPhysChem* **2024**, *25*, e202400581.
- (64) Chen, H.-Y.; Sheu, W.-S. *Journal of the American Chemical Society* **2000**, *122*, 7534–7542.
- (65) Messina, F.; Bräm, O.; Cannizzo, A.; Chergui, M. *Nature communications* **2013**, *4*, 2119.
- (66) Carter-Fenk, K.; Johnson, B. A.; Herbert, J. M.; Schenter, G. K.; Mundy, C. J. *The journal of physical chemistry letters* **2023**, *14*, 870–878.
- (67) Mitchell, P. *Nature* **1961**, *191*, 144–148.
- (68) Wikstrom, M. K. *Nature* **1977**, *266*, 271–273.
- (69) Rutledge, H. L.; Tezcan, F. A. *Chemical reviews* **2020**, *120*, 5158–5193.
- (70) Gray, H. B.; Winkler, J. R. *Annual review of biochemistry* **1996**, *65*, 537–561.
- (71) Blumberger, J. *Chemical reviews* **2015**, *115*, 11191–11238.
- (72) Ernster, L.; Dallner, G. *Biochimica et Biophysica Acta (BBA)-Molecular Basis of Disease* **1995**, *1271*, 195–204.
- (73) Vasconcellos, F. Illustration of the electron transport chain and the citric acid cycle in the mitochondria https://commons.wikimedia.org/wiki/File:Mitochondrial_electron_transport_chain%E2%80%944.svg.
- (74) Gutiérrez-Fernández, J.; Kaszuba, K.; Minhas, G. S.; Baradaran, R.; Tambalo, M.; Gallagher, D. T.; Sazanov, L. A. *Nature communications* **2020**, *11*, 4135.

- (75) Russell, W. J. *Chemical News and Journal of Physical Science* **1873**, 28, 148–153.
- (76) **2025**.
- (77) Chen, J.; Pelc, A.; Ameixa, J.; Kossoski, F.; Denifl, S. *ACS omega* **2024**, 9, 38032–38043.
- (78) Bull, J. N.; West, C. W.; Verlet, J. R. *Physical Chemistry Chemical Physics* **2015**, 17, 16125–16135.
- (79) West, C. W.; Bull, J. N.; Antonkov, E.; Verlet, J. R. *The Journal of Physical Chemistry A* **2014**, 118, 11346–11354.
- (80) Nonella, M. *Photosynthesis research* **1998**, 55, 253–259.
- (81) Gamiz-Hernandez, A. P.; Jussupow, A.; Johansson, M. P.; Kaila, V. R. *Journal of the American Chemical Society* **2017**, 139, 16282–16288.
- (82) Hartree, D. R. In *Mathematical Proceedings of the Cambridge Philosophical Society*, 1928; Vol. 24, pp 111–132.
- (83) Fock, V. *Zeitschrift für Physik* **1930**, 61, 126–148.
- (84) Szabo, A.; Ostlund, N. S., *Modern quantum chemistry: introduction to advanced electronic structure theory*; Courier Corporation: 1996.
- (85) Shavitt, I.; Bartlett, R. J., *Many-body methods in chemistry and physics: MBPT and coupled-cluster theory*; Cambridge university press: 2009.
- (86) Hohenberg, P.; Kohn, W. *Phys. Rev* **1964**, 136, B864.
- (87) Kohn, W.; Sham, L. J. *Physical review* **1965**, 140, A1133.
- (88) Sherrill, C. D.; Schaefer III, H. F. In *Advances in quantum chemistry*; Elsevier: 1999; Vol. 34, pp 143–269.
- (89) Čížek, J. *The Journal of Chemical Physics* **1966**, 45, 4256–4266.
- (90) Čížek, J. *Advances in chemical physics* **1969**, 14, 35–89.
- (91) Monkhorst, H. J. *International Journal of Quantum Chemistry* **1977**, 12, 421–432.
- (92) Raghavachari, K.; Trucks, G. W.; Pople, J. A.; Head-Gordon, M. *Chemical Physics Letters* **1989**, 157, 479–483.
- (93) Hättig, C.; Weigend, F. *The Journal of Chemical Physics* **2000**, 113, 5154–5161.
- (94) Emrich, K. *Nuclear Physics A* **1981**, 351, 379–396.
- (95) Stanton, J. F.; Bartlett, R. J. *The Journal of chemical physics* **1993**, 98, 7029–7039.

- (96) Krylov, A. I. *Annu. Rev. Phys. Chem.* **2008**, *59*, 433–462.
- (97) Jagau, T.-C.; Krylov, A. I. *The Journal of chemical physics* **2016**, *144*.
- (98) Melania Oana, C.; Krylov, A. I. *The Journal of chemical physics* **2007**, *127*.
- (99) Epifanovsky, E. et al. *J. Chem. Phys.* **2021**, *155*, 084801.
- (100) Dunning Jr, T. H. *The Journal of chemical physics* **1989**, *90*, 1007–1023.
- (101) Tao, J.; Perdew, J. P.; Staroverov, V. N.; Scuseria, G. E. *Physical review letters* **2003**, *91*, 146401.
- (102) Grimme, S.; Ehrlich, S.; Goerigk, L. *Journal of computational chemistry* **2011**, *32*, 1456–1465.
- (103) Zheng, J.; Xu, X.; Truhlar, D. G. *Theoretical Chemistry Accounts* **2011**, *128*, 295–305.
- (104) Weigend, F.; Ahlrichs, R. *Physical Chemistry Chemical Physics* **2005**, *7*, 3297–3305.
- (105) Schrödinger, LLC The PyMOL Molecular Graphics System, 2015.
- (106) Gozem, S.; Krylov, A. I. *Wiley Interdisciplinary Reviews: Computational Molecular Science* **2022**, *12*, e1546.
- (107) Gozem, S.; Krylov, A. I. *Chem. Lett* **2015**, *6*, 4532–4540.
- (108) Díaz-Tinoco, M.; Corzo, H. H.; Pawłowski, F.; Ortiz, J. *Molecular Physics* **2019**, *117*, 2275–2283.
- (109) Taguchi, A. T.; Mattis, A. J.; O'Malley, P. J.; Dikanov, S. A.; Wraight, C. A. *Biochemistry* **2013**, *52*, 7164–7166.
- (110) Taguchi, A. T.; O'Malley, P. J.; Wraight, C. A.; Dikanov, S. A. *Biochemistry* **2013**, *52*, 4648–4655.
- (111) De Almeida, W. B.; Taguchi, A. T.; Dikanov, S. A.; Wraight, C. A.; O'Malley, P. J. *The journal of physical chemistry letters* **2014**, *5*, 2506–2509.
- (112) Yuan, D.-F.; Liu, Y.; Zhang, Y.-R.; Wang, L.-S. *Journal of the American Chemical Society* **2023**, *145*, 5512–5522.

Appendix A

Algebraic expressions for the Dyson orbitals

EOM-EA-CC Dyson Equations

Right EOM-EA-CC Dyson orbital, $\phi_D^{\text{EA,R}} = \sum_i^{\text{occ}} \gamma_i^{\text{EA,R}} \phi_i + \sum_a^{\text{vir}} \gamma_a^{\text{EA,R}} \phi_a$:

$$\gamma_i^{\text{EA,R}} = \langle EA | \hat{a}_i^\dagger | CC \rangle \quad (1)$$

$$= l_a \quad (2)$$

$$\begin{aligned} \gamma_a^{\text{EA,R}} &= \langle EA | \hat{a}_a^\dagger | CC \rangle \\ &= - \sum_c t_{ic} l_c - \frac{1}{2} \sum_{kcd} t_{ki}^{dc} l_{dc}^k \end{aligned} \quad (3)$$

Left EOM-EA-CC Dyson orbital, $\phi_D^{\text{EA,L}} = \sum_i^{\text{occ}} \gamma_i^{\text{EA,L}} \phi_i + \sum_a^{\text{vir}} \gamma_a^{\text{EA,L}} \phi_a$:

$$\begin{aligned} \gamma_i^{\text{EA,L}} &= \langle CC | \hat{a}_i | EA \rangle \\ &= - \sum_c \lambda_{ic} r_c - \frac{1}{2} \sum_{kcd} \lambda_{ik}^{cd} r_k^{dc} \end{aligned} \quad (4)$$

$$\begin{aligned} \gamma_a^{\text{EA,L}} &= \langle CC | \hat{a}_a | EA \rangle \\ &= r_a + \sum_{kc} \lambda_{kc} r_{ca}^k + \sum_k \gamma_k^{\text{EA,L}} t_{ka} - \frac{1}{2} \sum_{klcd} \lambda_{lk}^{dc} t_{lk}^{da} r_c \end{aligned} \quad (5)$$

EOM-EA-EE-CC Dyson Equations

Right Dyson orbital, $\phi_D^{\text{EA-EE,R}} = \sum_i^{\text{occ}} \gamma_i^{\text{EA-EE,R}} \phi_i + \sum_a^{\text{vir}} \gamma_a^{\text{EA-EE,R}} \phi_a$:

$$\begin{aligned}
\gamma_i^{\text{EA-EE,R}} &= \langle EA | \hat{a}_i^\dagger | EE \rangle \\
&= r_0 \gamma_a^{\text{EA,R}} - \sum_c r_{ic} l_c - \frac{1}{2} \sum_{lcd} r_{il}^{cd} l_{dc}^l - \sum_{lcd} l_{dc}^l t_{ic} r_{ld}
\end{aligned} \tag{6}$$

$$\begin{aligned}
\gamma_a^{\text{EE-EA,R}} &= \langle EA | \hat{a}_a^\dagger | EE \rangle \\
&= r_0 l_a + \sum_{kc} l_{ca}^k r_{kc}
\end{aligned} \tag{7}$$

Left Dyson orbital, $\phi_D^{\text{EE-EA,L}} = \sum_i^{\text{occ}} \gamma_i^{\text{EE-EA,L}} \phi_i + \sum_a^{\text{vir}} \gamma_a^{\text{EE-EA,L}} \phi_a$:

$$\begin{aligned}
\gamma_i^{\text{EE-EA,L}} &= \langle EE | \hat{a}_i | EA \rangle \\
&= - \sum_c l_{ic} r_c - \frac{1}{2} \sum_{kcd} l_{ik}^{cd} r_k^{dc}
\end{aligned} \tag{8}$$

$$\begin{aligned}
\gamma_a^{\text{EE-EA,L}} &= \langle EE | \hat{a}_a | EA \rangle \\
&= \sum_{kc} l_{kc} r_{ca}^k + \sum_k \gamma_k^{\text{EE-EA,L}} t_{ka} - \frac{1}{2} \sum_{klcd} l_{lk}^{dc} t_{lk}^{da} r_c
\end{aligned} \tag{9}$$

EOM-IP-CC Dyson Equations

Right Dyson orbital, $\phi_D^{\text{EE,R}} = \sum_i^{\text{occ}} \gamma_i^{\text{IP,R}} \phi_i + \sum_a^{\text{vir}} \gamma_a^{\text{IP,R}} \phi_a$:

$$\begin{aligned}
\gamma_a^{\text{IP,R}} &= \langle CC | \hat{a}_a^\dagger | IP \rangle \\
&= \lambda_{ka} r_k + \frac{1}{2} \lambda_{lk}^{ca} r_{klc}
\end{aligned} \tag{10}$$

$$\begin{aligned}
\gamma_i^{\text{IP,R}} &= \langle CC | \hat{a}_i^\dagger | IP \rangle \\
&= r_i + \sum_{kc} \lambda_{kc} r_{ik}^c - \sum_c \gamma_c^{\text{IP,R}} t_{ic} - \frac{1}{2} \sum_{klcd} \lambda_{lk}^{dc} t_{li}^{dc} r_k
\end{aligned} \tag{11}$$

Left Dyson orbital, $\phi_D^{\text{IP,L}} = \sum_i^{\text{occ}} \gamma_i^{\text{IP,L}} \phi_i + \sum_a^{\text{vir}} \gamma_a^{\text{IP,L}} \phi_a$:

$$\begin{aligned}
\gamma_i^{\text{IP,L}} &= \langle IP | \hat{a}_i | CC \rangle \\
&= l_i
\end{aligned} \tag{12}$$

$$\begin{aligned}
\gamma_a^{\text{IP,L}} &= \langle IP | \hat{a}_a | CC \rangle \\
&= \sum_k t_{ka} l_k + \frac{1}{2} \sum_{klc} t_{kl}^{ac} l_{kl}^c
\end{aligned} \tag{13}$$

EOM-EE-IP-CC Dyson Equations

Right Dyson orbital, $\phi_D^{\text{EE-IP,R}} = \sum_i^{\text{occ}} \gamma_i^{\text{EE-IP,R}} \phi_i + \sum_a^{\text{vir}} \gamma_a^{\text{EE-IP,R}} \phi_a$:

$$\begin{aligned}
\gamma_i^{\text{EE-IP,R}} &= \langle EE | \hat{a}_i^\dagger | IP \rangle \\
&= \sum_{kc} l_{kc} r_{ik}^c - \sum_c \gamma_c^{\text{IP-EI}} t_{ic} - \frac{1}{2} \sum_{klcd} l_{lk}^{dc} t_{li}^{dc} r_k
\end{aligned} \tag{14}$$

$$\begin{aligned}
\gamma_a^{\text{EE-IP,R}} &= \langle EE | \hat{a}_a^\dagger | IP \rangle \\
&= l_{ka} r_k + \frac{1}{2} l_{lk}^{ca} r_{klc}
\end{aligned} \tag{15}$$

Left Dyson orbital, $\phi_D^{\text{IP-EE,L}} = \sum_i^{\text{occ}} \gamma_i^{\text{IP-EE,L}} \phi_i + \sum_a^{\text{vir}} \gamma_a^{\text{IP-EE,L}} \phi_a$:

$$\begin{aligned}
\gamma_i^{\text{IP-EE,L}} &= \langle IP | \hat{a}_i | EE \rangle \\
&= r_0 l_i + \sum_{kc} l_{ik}^c r_{kc}
\end{aligned} \tag{16}$$

$$\begin{aligned}
\gamma_a^{\text{IP-EE,L}} &= \langle IP | \hat{a}_a | EE \rangle \\
&= r_0 \gamma_a^{\text{IP,L}} + \sum_k r_{ka} l_k + \frac{1}{2} \sum_{klc} r_{kl}^{ac} l_{kl}^c + \sum_{klc} l_{kl}^c t_{ka} r_{cl}
\end{aligned} \tag{17}$$

Appendix B

Photoelectron Cross-sections

TODO: add all gnuplot figures.

Quantum Chemistry and Physical Chemistry

Celestijnenlaan 200F bus 2404

3001 LEUVEN, BELGIË

tel. + 32 16 37 21 98

jeremy.harvey@kuleuven.be

www.kuleuven.be

